JOURNAL OF THERMOPHYSICS AND HEAT TRANSFER
Vol. 33, No. 2, April–June 2019

Design to Validation of a New Heat Flux Source with Uncertainty Analysis

Jay I. Frankel,* Hongchu Chen,† and Kevin Mathew‡
University of Tennessee, Knoxville, Tennessee 37996-2210

DOI: 10.2514/1.T5519

High-speed, transient aerothermal studies produce excessive temperatures and heat fluxes in laboratory, ground, and flight-test experiments. Experiments are performed for 1) understanding the response of test vehicles under various induced thermal environments, 2) verifying computational codes and input parameters, and 3) evaluating thermophysical and mechanical characteristics of new materials. In addition to these rationales, the reconstruction of the surface heat flux from in-depth or backside instrumentation is an important inverse application. Recent research has led to an alternative view of inverse heat conduction based on calibration principles performed in the frequency domain leading to a novel "parameter-free" inverse heat conduction measurement equation. The final mathematical framework reveals that the resolution of a first-kind Volterra integral equation for the surface heat flux prediction contains only experimental data sets. This type of mathematical formulation is highly ill posed. This paper focuses on the design, fabrication, and preliminary test campaign of a new electrical heating cell for producing a verifiable heat flux source. The feasibility investigation demonstrates the merits of system through modeling, experimental design, and transient uncertainty propagation. Validation studies are presented, leading to favorable outcomes. Slug calorimetry, composed of a pure copper, is used in the validation campaign.

Nomenclature

A	=	constant, $s^{-1/2}$
A_s	=	cross-sectional surface area, 25.4×25.4 mm
A_t	=	wetted surface area, m^2
C	=	heat capacitance, J/K
C_0	=	coefficient, J/K
C_1	=	coefficient, J/K^2
C_2	=	coefficient, J/K^3
C_3	=	coefficient, J/K^4
c_p	=	specific heat, $J/(kg \cdot K)$
I	=	current, A
k	=	thermal conductivity, $W/(m \cdot K)$
m	=	mass, kg
P	=	power, W
P_0	=	power magnitude, W
Q	=	power or energy rate, W
q''	=	heat flux, W/m^2
R	=	resistance, Ω
$\overline{R}$	=	sum square of the residuals, W^2
r	=	residual, W
T	=	temperature, K or °C
T_0	=	temperature initial condition, K or °C
t	=	time, s
t_{off}	=	time at which power is turned off, s
$t_{\max}$	=	maximum time for experiment, s
U	=	voltage, V
u	=	dummy time variable, s
Z	=	sensitivity function (appropriate units)
β	=	geometric correction factor [in Eq. (18)]
$\overline{\beta}$	=	geometric correction factor [in Eqs. (19b) and (19c)]
Γ	=	$\overline{\gamma} A_s$, $m \cdot s^{1/2}$
$\overline{\gamma}$	=	$1/\sqrt{\alpha_{\text{INS}}\pi}$, $s^{1/2}/m$
γ_0	=	coefficient, $(W \cdot s^{1/2})/K$
γ_1	=	coefficient, $(W \cdot s^{1/2})/K^2$
η	=	arbitrary coordinate system
θ	=	heating rate, K/s or °C/s
λ	=	coefficient, $J/(K \cdot s^{1/2})$
$\overline{\lambda}$	=	coefficient, $J/(m^2 \cdot K \cdot s^{1/2})$
μ	=	parameter for voltage profile, s
ρ	=	density, kg/m^3
σ	=	parameter for voltage profile, s
Φ	=	property (parameter) defined for uncertainty analysis, slug
ϕ	=	property (parameter) defined for uncertainty analysis (heater)
Ψ	=	modified sensitivity function (appropriate units)

Subscripts

AlN	=	aluminum nitride
BULK	=	bulk
Cu	=	copper
gen	=	generation
H	=	heater
INS	=	insulation
in	=	in
m	=	measured value
out	=	out
SP	=	silver paste
TF	=	thin-film thermocouple

Presented as Paper 2018-0983 at the 2018 AIAA Aerospace Sciences Meeting, Kissimmee, FL, 8–12 January 2018; received 4 May 2018; revision received 31 August 2018; accepted for publication 24 October 2018; published online 31 December 2018.

*Ph.D. Professor, Department of Mechanical, Aerospace, and Biomedical Engineering; jfranke1@utk.edu. Associate Fellow AIAA (Corresponding Author).

†Ph.D. Research Associate, Department of Mechanical, Aerospace, and Biomedical Engineering.

‡Undergraduate Research Assistant, Department of Mechanical, Aerospace, and Biomedical Engineering.

I. Introduction

THE availability of accurate and cost-effective heat flux sources is mandated for calibration purposes that cover a gamut of design space conditions involving temperature, heating rate (degrees Celsius per second), and heat flux (Watts per square meter). Two obvious purposes for such a facility involve 1) the calibration of heat flux gauges, and 2) verifying inverse heat conduction analyses that can effectively serve as a surface (net) heat flux gauge. Caution is also required because no single source will most likely cover the entire design space involving the full spectrum of spatial and temporal scales that take place in aerospace application [1–11]. Many laboratory-based, high-temperature, and high-heat flux sources have

been reported in the literature involving quartz lamps, lasers, electrical heaters, etc. Ground-test facilities for high-speed flow emulation include arcjets, plasmatrons, lasers, solar facilities, etc. Most laboratory facilities are quite expensive to construct and maintain. Further, the best estimation of a sample's surface (net) heat flux involves the understanding of model and measurement uncertainties and often requires the introduction of correction procedures for acquiring the best evaluation of this quantity.

Inverse heat conduction analysis [12–14] leads to a collective instrumentation/analysis approach for estimating the surface (net) heat flux in a sample or plug. Inverse problems are ill posed [15–17] and require special mathematical tools for resolving a stable and accurate prediction. This approach represents a practical means for estimating the surface thermal condition (i.e., surface heat flux and/or surface temperature) while protecting the integrity of the measurement device or sensor as it lays in depth to the sample. In this scenario, the sensor remains at a safe distance from the active source to retain reliable data and assuring no sensor damage or changes in the installation. Conventional "parameter-required" methods require accurate input parameters involving thermophysical properties, probe positioning, and probe characteristics (e.g., thermocouple time constant and proper accounting of conductive lead losses [18,19]). For example, significant thermocouple time constants (greater than 2 s) have been reported in the literature [20] that, left unaccounted, substantially attenuate and time delay the predicted surface temperature and heat flux [18,19]. Unlike parameter-required methods, the recently proposed calibration integral equation method [21–31] is a parameter-free advance for resolving inverse heat conduction problems. It is predicated on the accurate specification of the surface (net) heat flux from a calibration campaign before later reconstructions resulting from environmental tests.

Parameter-required [12–14] and parameter-free [10,11,22–27,32–35] inverse heat conduction methods require careful and meticulous validation. In parameter-required methods, the measured in-depth temperatures or a combination of in-depth measurement with known backside boundary condition are projected to the front surface and compared to the experimentally imposed front surface heat flux. Thermophysical properties of the test material, positions of the thermocouples (TCs), and characterization of the thermocouples require accurate specification as input parameters to this inverse algorithm. A parameter-free method removes the need to specify these parameters. That is, the method is based on a series of calibration studies with known surface boundary condition and measured in-depth temperature data. In this case, it is assumed that the system properties do not change. For example, the thermocouple adhesive does not degrade or loosen the TC during a series of tests. Of course, this assumption is inherent to all repeated studies. The mathematical formulation removes the need to specify the thermophysical properties, sensor positions, and sensor characteristics in lieu of experimental data. In this case, a measurement equation is produced that is mathematically stated by a first-kind Volterra integral equation involving the reconstruction surface (net) heat flux. All inverse techniques require the introduction of a regularization method for stabilizing the highly ill-posed nature of the inverse problem. With the parameter-free method, the onus is placed on accurate calibration campaigns in which either or both the surface (net) heat flux or temperature are well characterized throughout the transient process.

This paper proposes developing a small-sample, high-heat flux facility capable of producing the heat fluxes and temperature ranges described in Ref. [36] at a fraction of the cost while substantially reducing physical complications. The present phase illustrates several novel concepts for the feasibility study while producing temperature results in the range of [0, 300]°C. This present temperature limitation is due to the interfacial grease that will shortly be replaced with a high-temperature, electrical insulator substitute. In the second phase of studies, the desired temperature range lies in [0, 450]°C with a maximum heat flux of approximately 100 W/cm^2. This proposed configuration uses conventional laboratory test equipment normally stocked in well-equipped laboratory environments. Key to this approach is the availability of turn-key designed instrumented aluminum nitride (AlN) heaters available and manufactured by Oasis Materials, Inc. [37] and Durex Industries [38]. AlN represents the substrate and does not describe the heating element or the in-depth instrumentation (i.e., industry standard term is "trace" for depicting the in-depth heating element and instrumentation [37,38]). In this paper, an initial systematic investigation is presented describing both the merits and hurdles associated with these heaters for extracting the departing heat flux. This process requires careful experimental design and modeling considerations.

This paper is divided into three additional sections. Section II provides a brief review on choices for a heating source. Section III discusses eight technical features of the design process leading to the prediction outcomes. This section includes modeling, sensitivity analysis, heat flux predictions, and uncertainty propagation based on fixed model. Finally, Sec. IV concludes the study with comments on the preliminary design and outcomes.

II. Heating Source Choice for Consideration, Modeling, and Experimental Design Concepts

The development of a small-sample, rapid-turnaround test facility is of significant interest to the aerospace community for plug development, material evaluation, and sample assessment for potential TPS applications. Instrumented samples could be composed of pedigreed materials (e.g., aluminum, copper, stainless steel 304), ultrahigh-temperature ceramics, or composite (e.g., C/C or C/C-SiC) materials.

A well-defined heating source is also necessary for the calibration stage of a parameter-free inverse method or for verifying a parameter-required inverse method. For the latter case, this is also an important step before implementation because significant uncertainties can exist in defining the thermophysical properties, probe locations, and sensor behavior. Several choices are available for defining a well-characterized source. The choice depends on the design space requirements (e.g., test duration, heat flux and temperature ranges, heating rate), costs and availability of the source, desired accuracy, stability, repeatability, etc. Lasers [30,31] and electrical heaters [21] are two commonly available heating sources. With regard to physical heat flux gauges, Blanchat and Hanks [36] compare several heat flux gauges for accuracy and performance. Lasers are repeatable, monochromatic sources but require spectral and temperature characteristics of the sample's surface (both the spectral absorptivity at the laser wavelength and surface temperature as well as total hemispherical emissivity at the surface temperature are required). Uncertainties can be reduced by introducing a surface coating such as Pyromark 2500 paint, which is both spectrally and temperature-dependently well studied [39]. Alternatively, an electrical heating source can be used that is in direct contact with the sample. This alleviates the need to know the radiative properties but introduces contact resistance between the heater and sample surface, which can reduce the effectiveness of the heat transfer. Off-the-shelf electrical heaters are available (e.g., Watlow Electric Ultramic ceramic heater 240 V, 967 W with single in-depth, near-edge thermocouple), but their quantifications are difficult to establish because they are not well designed for estimating the heat flux as required by this application. Symmetric heating such as defined by a sandwich configuration involving the heater "sandwiched" between two identical samples is often problematic in obtaining actual symmetry and accounting for the storage of energy in the heater. Energy storage is often neglected, which could lead to misleading results.

III. Initial Procedure for Characterizing Heat Flux and Quantifying Test Facility

The procedure described in this paper follows the outline given next.

1) Design the heater with resistance temperature detector (RTD) instrumentation and lead connections for a specific temperature and heat flux range. The internal RTDs are used for estimating the bulk temperature of the heater. Energy storage is included in the model to be described in later sections.

2) Define required instrumentation based on available laboratory inventory.

3) Calibrate internal heater RTDs in a passive (nonactivated) means through a series of steady-state experiments. Repeatability studies are performed for estimating the error bound in these temperature measurements. A high degree of accuracy is not required. This provides the necessary resistance versus temperature curve fit, whose coefficients can be implemented into a data acquisition (DAQ) system. The tungsten heater trace is also calibrated by measuring its resistance over temperature. This can be used in postprocessing the data to provide an extra temperature data stream.

4) Define the mathematical model based on sound fundamental assumptions. This model will contain several unknown thermophysical parameters that depend on temperature. Additionally, the heater is not composed of an isotropic material.

5) Devise the experiment and test cell for extracting parameters based on sensitivity analysis for defining the "best" power input for extracting the unknown parameters.

6) Modify the model equation and test cell for performing experiments where the exiting heat flux is now available and quantified through the model.

7) Design a comparison experiment for validation purposes. For the present study, a slug calorimeter composed of copper demonstrates the merit of the entire process and facility.

8) A classical uncertainty propagation analysis is performed based on a fixed model for understanding the transient uncertainty behavior. The heater and slug model equations are considered in the uncertainty analysis.

A. Heater Choice and Characterization

Figures 1–3 display the custom AlN heater fabricated by Oasis Materials, Inc. The AlN portion of the heater descriptor refers to the substrate. These heaters possess a tungsten heating element, known as a trace, and two tungsten RTD traces, per Figs. 2 and 3. For this initial investigation, a 25.4×25.4 mm cross-sectional area heater is proposed. The thickness of the heater is 1.02 mm. As seen in Figs. 1 and 2, delicate lead pins exist for the power supply and two tungsten RTDs. The RTD traces are located above and below the tungsten heater trace (Fig. 3 provides a cross-sectional cut showing through-the-thickness measurements for Fig. 2). The x ray displayed in Fig. 2 shows the intricate manufacturing associated with this heater. The provided RTDs were not calibrated and thus required in-house calibration.

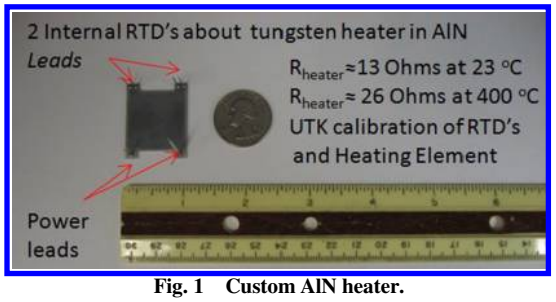

Fig. 1 Custom AlN heater.

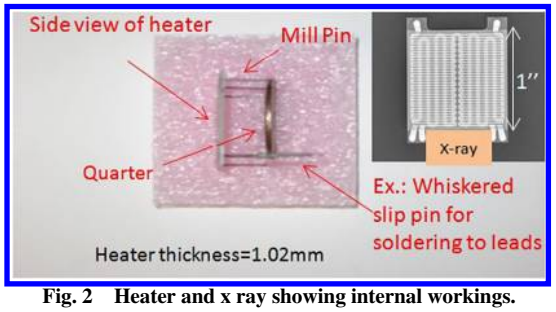

Fig. 2 Heater and x ray showing internal workings.

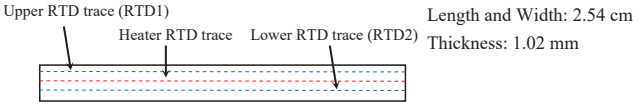

Fig. 3 Drawing for the Oasis heater [37].

B. Instrumentation

Table 1 provides the instrumentation, insulation, and other items used in the experimental study [40–47]. These items are not optimized but readily available at a reasonable cost.

C. Resistance Temperature Detector and Heater Resistance Calibration

The resistance calibration is performed through a series of conventional steady-state experiments in which heat is supplied by the hot plate shown in Fig. 4. In this case, one-dimensional heat steady-state conduction is assumed, such that $q'' = -k(dT/dx)$. Waiting until the thin-film thermocouple temperature becomes constant establishes the steady-state condition in the heater (without power supplied to the heater). A resistor analogy then becomes available for later use. This test cell consists of a machined aluminum base plate ($5.08 \times 5.08 \times 0.635$ cm) with heater seat (machined to depth 1.02 mm, and sized to account for thermal expansion mismatch which is necessary), AlN heater, a layer of Pyrogel [40], and an aluminum cover plate that is sandwiched and bolted (hand tightened). A type K exposed bead thermocouple probe (0.02 in.) is inserted into a centered drilled hole (in all directions) of diameter 0.061 cm and adhered using AREMCO 669 adhesive. The high thermal conductivity of aluminum and steady-state measurements are intended to justify that the in-depth aluminum placed TC represents the aluminum temperature. This TC is merely used as an additional temperature check on the thin-film TC (no thermodynamic violations).

It is important to note the purpose of knowing the internal temperatures of the heater. These measured temperatures could establish or help define the bulk heater temperature of the aggregate substrate composed of AlN and tungsten. This bulk temperature will later be used in a proposed model for estimating the temperature-dependent heat capacitance of the manufactured heater. With this said, the accuracy of ±2–3°C is sufficient and easily achievable. The calibration is performed using a type K thin-film (TF) thermocouple adhered to the pin-side of the heater. As such, the exposed thin-film thermocouple ribbons are not electrically isolated further. The front-face to back-face heater temperature difference ΔT can be estimated with the aid of Fourier's law and an estimate of heat flux from the hot plate while assuming an AlN or Tungsten or weighted AlN/Tungsten thermal conductivity. The upper-bound estimate for the temperature difference is 1–2°C. The test procedure is conventional as the hot plate's temperature is set and steady state is reached in the heater and aluminum block after sufficient time (about 1 h for each data point). The corresponding resistance measurement is made using a Data Translation (DT) 9829 data acquisition board. The process involves setting the set-point temperature of the hot plate and waiting until steady state is achieved (monitoring the thin-film temperature). A resistance measurement of each RTD is then recorded for this steady-state condition corresponding to the thin-film temperature. The process is continued by increasing the hot-plate set-point temperature in 50°C increments until the desired temperature span is covered. This steady-state campaign produces highly repeatable results for the RTDs and tungsten heating element. Figures 5a and 5b reveal results from three test runs verifying good repeatability for the RTDs, whereas Fig. 6 displays the resistance measurements taken at the same time for the tungsten heater trace.

The dominant material in the heater displayed in Figs. 1 and 2 is AlN. AlN possesses strongly temperature-dependent thermophysical properties [48,49]. The thermal conductivity decreases with increasing temperature, whereas the specific heat increases with increasing temperature. It is extremely important to account for thermal expansion in the aluminum base plate seat because this omission in the design of holders can prove disastrous due to mismatch expansion at elevated

Table 1 Itemization of experimental components

Item	Model number	Purpose	Additional information
Pyrogel insulation [40]	Aspen Aerogel- Pyrogel XT-E	Insulation for resistance measurement cell	$T < 650$°C
DAQ [41]	DT-9829	Multimeasurement data acquisition for synchronized production of data	Eight channels: voltage, current, RTD, thermocouples
Power supply [42]	Keysight model N5700	Programmable dc power supply	$U < 150$ V, $I < 10$ A
Hot plate [43]	Cole-Parmer EW-03405-10	Calibration of RTDs and heater trace (resistance as function of temperature)	$T < 540$°C, $q'' < 3.3$ W/cm^2
Insulation [44]	ZIRCAR MICROSIL	Insulation used in all tests, thickness = 12.5 mm	$0.019 < k < 0.028$ W/(m · K), $\rho = 230$ kg/m^3, $c_p = 800$ J/(kg · K)
Thin-film thermocouples [45]	OMEGA CO2-K, type K	Thin-film type K thermocouple	Thickness = 0.0005 in., $T < 500$°C recommended
RTD extension wire [46]	EXGG-2CU-20	RTD extension wire	$T < 482$°C, solid braid insulation/glass
Oscilloscope	Tektronix TDS 2014B	Verifying voltage/currents at bus bar	100 MHz
Mass measurements	Sartorius TE214S	Measure mass	— —
Adhesive	AREMCO 669 cement	Thin film to surface	$T < 1000$°C, thickness = 5 mm
Thermocouple probe [47]	OMEGA TMTIN-020E-3, type T	Exposed bead for estimating penetration time in the insulation	$T < 400$°C
LabView	Version 2016	Control of voltage output of the dc power supply	— —
AREMCO thermal paste	Heat-Away 641 silver paste	Contact reduction grease	$T < 280$°C[a]
Blanket insulation	ISOFRAX C8PCF-1/2 in. PS-0017	Gap insulation	$T < 1260$°C

[a]New customized product by AREMCO will be tested, $T < 815$°C.

temperatures. Again, this preliminary heater possesses a design limit of approximately 400°C sustained.

It should be noted that the curve fits shown in Fig. 5 are mapped onto the Callendar–Van Dusen [50] form, whose resulting coefficients are then inserted into the DT9829 DAQ's custom mode for RTD conversions. A direct curve-fit routine based on the Callendar–Van Dusen form could also be developed. The heater resistance is extracted in a different manner as the voltage U and current I are measured, leading to the power P calculation. With known power and say known voltage, the resistance at any instant in time can be calculated from $P(t) = U(t)^2/R[T(t)]$, or use $U(t) = I(t)R[T(t)]$. An estimation of the tungsten heater temperature can be recovered as the heater temperature is also collected at the same instant in time and estimated from the thin-film thermocouple. Figure 6 shows that the heater's resistance dependency on temperature produces less sensitivity than the RTDs (as expected). However, this calculation can be useful for many qualitative and quantitative purposes. This passive approach (power off) helps identify flaws in the construction of the heater/instrumentation/material when used actively (power on) because both the interior RTD temperature predictions should not drastically divert from the TF thermocouple temperature measurement.

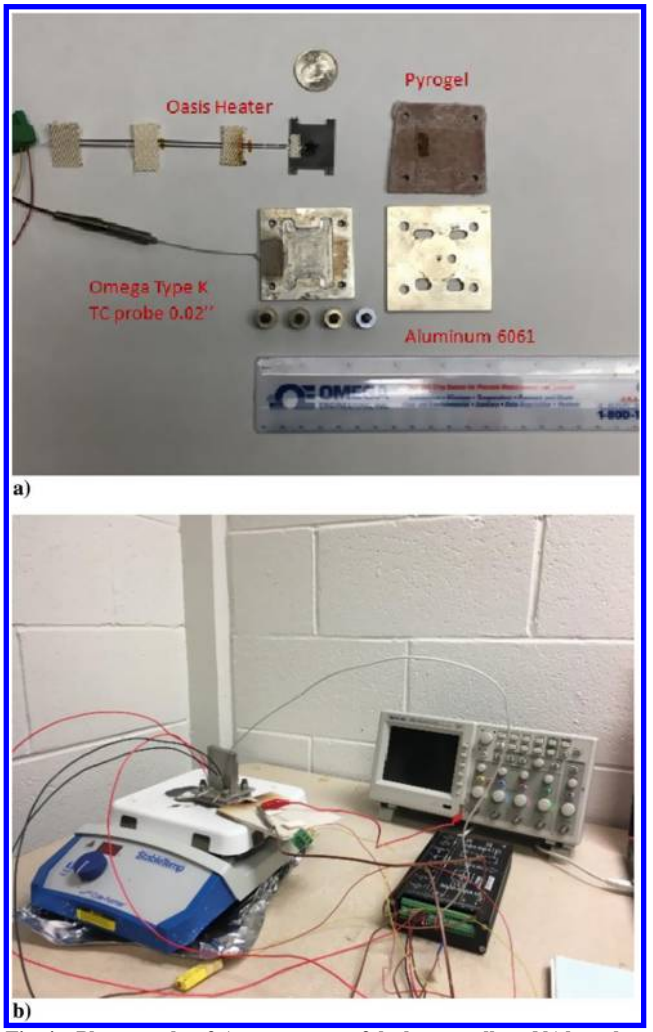

Fig. 4 Photographs of a) components of the heater cell, and b) hot-plate setup for measuring electrical resistance.

Before proceeding further, it should be noted that the RTDs produced spurious results at high-temperature and high-power inputs due to current leakage from the heater somehow flowing into the RTDs. This unfortunate occurrence or flaw was reported to the manufacturer, and a new generation of heaters will not produce this adverse effect. However, the procedures of this section remain valid. It is important to check this when the heater is under load. The procedure is to deactivate, say, the RTD in the pin side of the heater (designated as RTD2) from the DAQ current (425 mA, NT 9829) and directly measure current flow in the RTD using the DAQ. The RTD in the opposite of the pin side is designated by RTD1. Figure 7 shows a typical example of the current contamination to the RTD. Here, a constant 2 A current is supplied to the heater until termination or shut off at approximately 18 s. For this test, the surrounding heater environment is composed of ZIRCAR's MICROSIL [44] insulation. The attached type K thin-film thermocouple temperature at the time of power termination was approximately 310°C.

At a temperature above 300°C, the current leakage into the RTD becomes nonnegligible relative to the DAQ driving RTD current. As the power of the heater increases, this phenomenon is readily seen at lower temperatures. However, in many tests, the results were quite good and indicated the merit of the RTDs for future studies because the bulk temperature of the heater can be established to a better accuracy than merely using the thin-film thermocouple temperature attached to the heater's pin side.

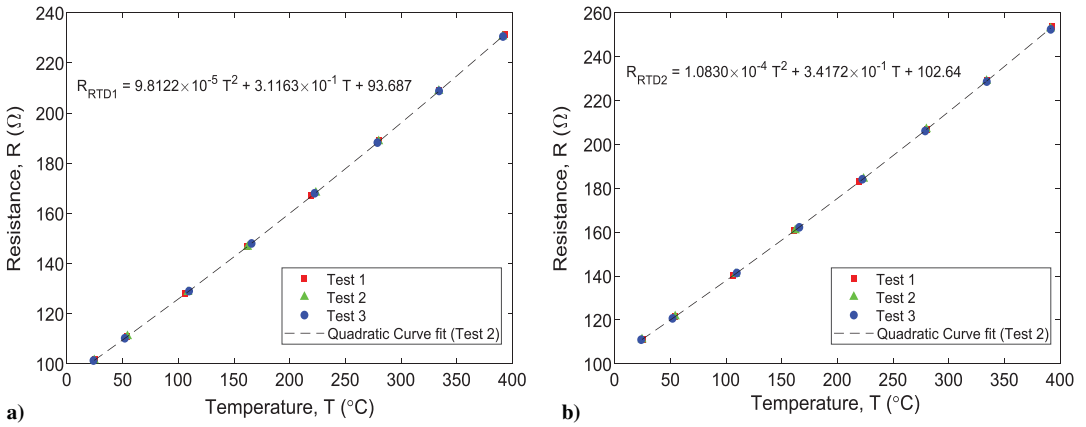

Fig. 5 Resistance measurements: a) RTD 1 (opposite of the pin side), and b) RTD 2 (pin side) resistance vs thin-film temperature.

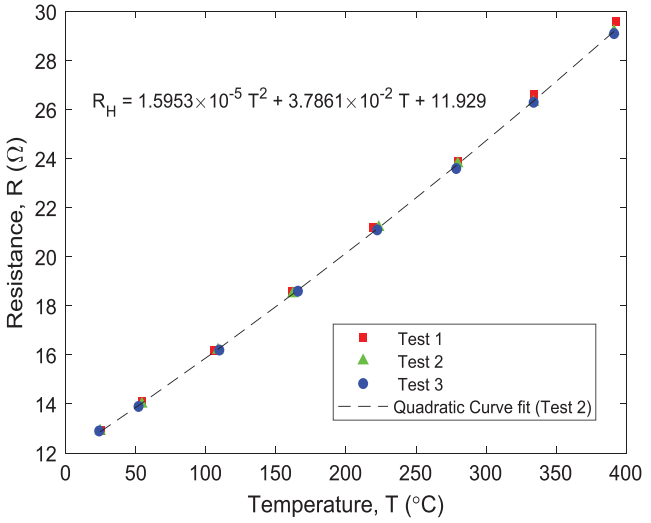

Fig. 6 Heater resistance as a function of thin-film temperature.

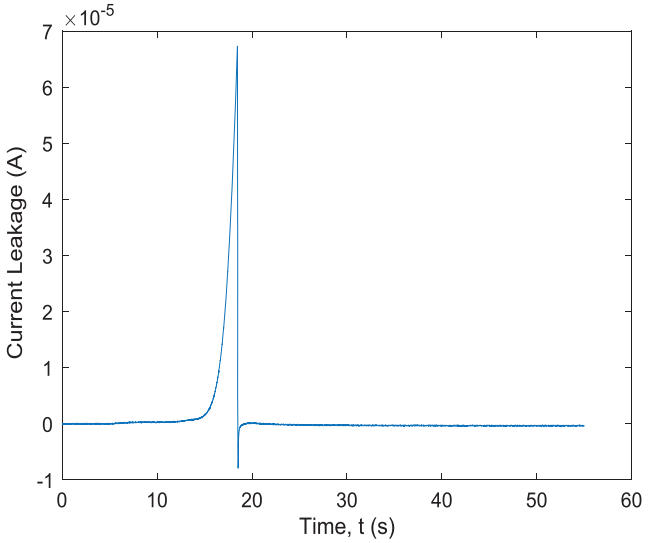

Fig. 7 Measured current in RTD when power is applied (power shut off at ~18 s).

D. Mathematical Modeling and Sensitivity Analysis for the Experimental Design Process

Aluminum nitride possesses a high thermal conductivity at room temperature (≈150–300 $W/(m \cdot K)$ depending on the reference source) that decreases with increasing temperature. For this preliminary investigation, a lumped system approach is taken whereby an effective (or average or bulk) temperature can be defined.

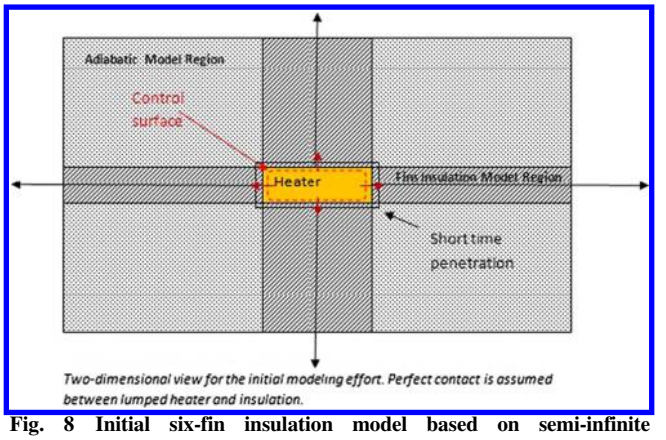

Fig. 8 Initial six-fin insulation model based on semi-infinite approximation.

As previously noted, at this juncture, four distinct temperature measurements in the 1.02-mm-thick AlN heater are available (two RTDs, one heater, and one thin-film TC on the pin side). Further discussion on the measurement used to represent the bulk temperature is held until a later section. With this definition of temperature, a heat capacitance function can be constructed using a parameter-estimation approach. In this component of the procedure, the heater is encased in insulation composed of ZIRCAR's MICROSIL [44]. The insulation thermal effusivity coefficient will also be approximated but based on the thin-film thermocouple temperature. A novel six-fin formulation is initially considered as shown in Fig. 8 for 1) evaluating the heater's thermal symmetry, and 2) forming the initial heat capacitance and thermal effusivity estimates. Each fin (in three-dimensional space, two are not shown) is assumed ideally semi-infinite in length and adiabatically isolated, as noted in Fig. 8. This leads to one-dimensional (fin) heat conduction when the surface in contact with the heater is at a spatially uniform temperature. Under this simplification, an integral relationship between the fin entering heat flux and fin surface temperature exists when constant properties are assumed in the fin [22]. Multidimensional effects are assumed small because the thermal front has not deeply penetrated into the insulation (note corner effects in Fig. 8). Voltage (or current) inputs will be programmed to the heater (through LabView), and time histories of the heater's element temperature, RTD temperatures, and thin-film thermocouple temperature will be studied. ZIRCAR's MICROSIL [44] insulation is chosen because its reported thermal conductivity lies in the range of 0.019–0.028 $W/(m \cdot K)$ for the proposed temperature range of interest. Additionally, this is not a structural insulation and thus permits compliance under light compression for reducing contact resistance. An OMEGA type T thermocouple probe (0.02 in., exposed bead) is placed on the top-side exposed insulation (and covered) region of the test cell for assuring the semi-infinite assumption in the proposed time span of the experiments. This geometry also provides physical insight into the instrumentation and transient responses of the sensors.

Many important studies involve only 10–120 s of test time. In this brief period, the maximum temperature will be produced. Recall that the insulation thickness is merely 12.5 mm.

Before describing the modeling process, Figs. 9a and 9b show the physical configuration in which the heater is sandwiched in the insulation cell. Figure 10 displays the tabletop experiment. A series of steps are defined and investigated for evaluating and characterizing the custom designed heater composed of a tungsten trace heating element within an aluminum nitride (AlN) substrate possessing two RTDs traces located above and below the heating element, as shown in Figs. 1 and 2. This represents a complicated arrangement in which a design space must be defined for assuring accuracy under certain system constraints. The focus for this preliminary study, based on possessing limited resources, involves characterizing the energy storage and heat losses to the insulated cell. This identical insulation will be used in the next test segment involving the establishment of

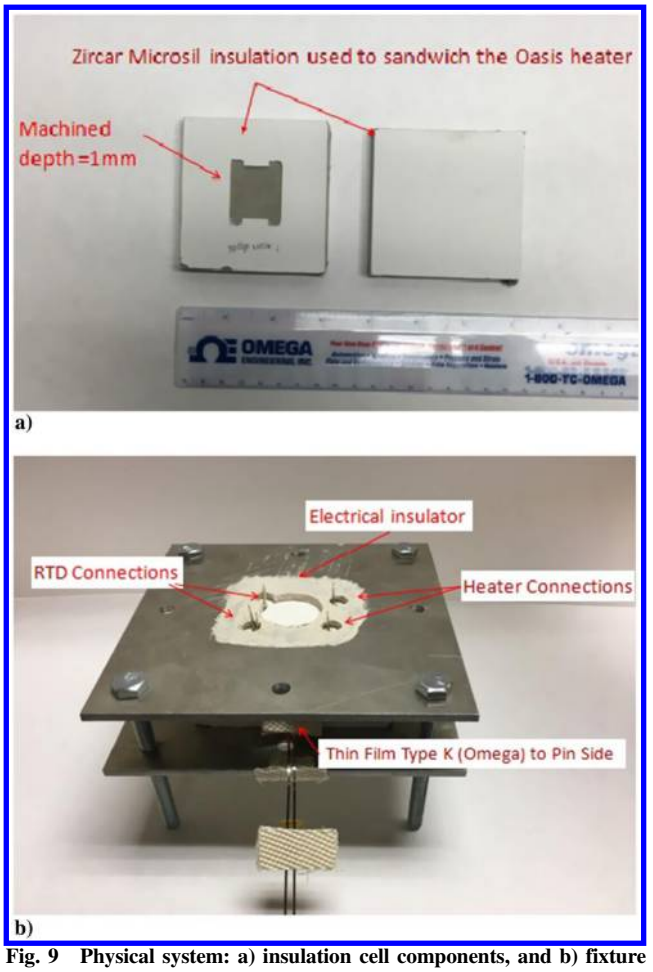

Fig. 9 Physical system: a) insulation cell components, and b) fixture holder.

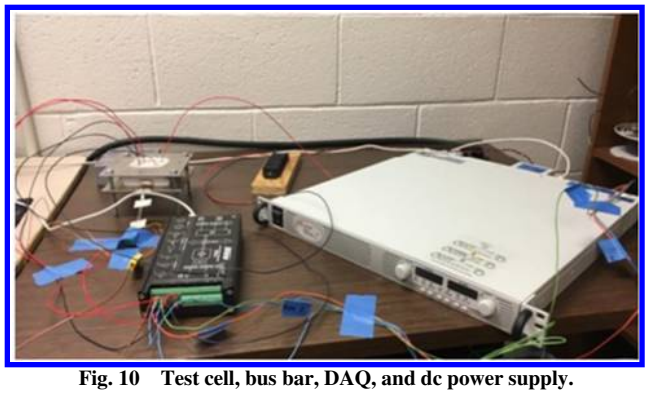

Fig. 10 Test cell, bus bar, DAQ, and dc power supply.

the heat loss from the heater in a one-sided (not sandwiched) test arrangement. The parameters to be extracted are associated with the heater's heat capacitance and insulation thermal effusivity.

A sequential and well-orchestrated investigation based on in-depth sensor calibrations, simplified modeling, parameter estimation, and sensitivity analyses will be emphasized for extracting two key properties of the system. A design space will be defined whereby all heating scenarios must lie to assure a high degree of heat flux accuracy. The Oasis Heater can produce a maximum one-sided heat flux in the range of 80–140 $\mathrm{W/cm^2}$ (recall that tungsten resistivity is temperature-dependent).

The following are assumptions in the modeling process.

1) An idealized six-fin model is assumed about the heater with one-dimensional heat transfer in the semi-infinite insulation region.

2) Temperature-dependent heat capacitance is assumed based on a bulk heater temperature.

3) Constant thermophysical properties are assumed in the insulation.

4) All fins have identical transient base temperature.

5) Lumped energy balance is assumed in terms of bulk temperature and fin surface temperature.

6) As noted earlier, the RTDs are deemed unreliable, and hence the thin-film thermocouple is presently used for estimating the bulk temperature. Some results using the RTD will be shown indicating merit of this instrumentation.

7) Perfect thermal contact is assumed between the heater and insulation.

A control volume, lumped analysis of heat transfer in the heater shown in Fig. 8 leads to

$$\sum Q_{\text{in}} + Q_{\text{gen}} = \sum Q_{\text{out}} + Q_{\text{stor}} \ \text{(W)} \tag{1}$$

The heat flux in the semi-infinite (insulated) fin regions is described by [22]

$$q''_{\eta}(\eta = 0, t) = \bar{\lambda} \int_{u=0}^{t} \frac{\partial T_{\text{INS}}}{\partial u}(\eta = 0, u) \frac{du}{\sqrt{t-u}}, \qquad t \geq 0 \tag{2}$$

where

$$\bar{\lambda} = \frac{\sqrt{\rho_{\text{INS}} c_{p,\text{INS}} k_{\text{INS}}}}{\sqrt{\pi}}$$

As indicated in Fig. 8, it is assumed that the corners are modeled as adiabatic regions. It is presently assumed that this leads to a second-order effect based on the provided assumptions. Substituting Eq. (2) into the energy balance given in Eq. (1) as defined for the control volume of the heater produces

$$P(t) = C(T_{\text{BULK}}(t)) \frac{dT_{\text{BULK}}}{dt}(t) + \lambda \int_{u=0}^{t} \frac{\partial T_{\text{INS}}}{\partial u}(\eta = 0, u) \frac{du}{\sqrt{t-u}}, \qquad t \geq 0 \tag{3}$$

where $\lambda = \bar{\lambda} A_t$, and $C(T_{\text{BULK}}(t)) = m_H c_{p,H}(T_{\text{BULK}}(t))$. Here, A_t is the wetted area of the heater. Based on the assumptions that

$$T_{\text{INS}}(\eta = 0, t) = T_{\text{AlN,surface}}(t) = T_{\text{TF}}(t) \tag{4}$$

where TF = thin film, Eq. (3) further reduces to

$$P(t) = C(T(t)) \frac{dT}{dt}(t) + \lambda \int_{u=0}^{t} \frac{dT_{\text{TF}}}{du}(u) \frac{du}{\sqrt{t-u}}, \qquad t \geq 0 \tag{5}$$

where $T(t) = T_{\text{BULK}}(t)$, and $T(0) = T_0$. The definition of bulk temperature will again shortly be described for the physical experiment due to RTD reliability issues.

At this junction, several pertinent observations must be related because the unknowns in this equation involve $C(T)$ and λ.

The power $P(t)$ is measured [leading to $P_m(t)$] with its inherent uncertainties. The time derivative of the measured temperature is required, which contains both measurement and truncation errors. Finally, there is the proposed model that inherently possesses errors deviating from reality.

E. Test Procedure Based on Sensitivity Analysis

Before proceeding, the first question that naturally arises involves which profile of $P(t)$ will produce a beneficial temporal event for extracting $C(T)$ and λ. Not all profiles can extract the true parameters. It is recommended to gain insight into the parameter estimation process by introducing a simple constant property model as an exact analytic solution is available. This allows the sensitivity coefficients to be viewed in terms of parameter dependencies.

1. *Sensitivity Analysis: Constant Properties*

Let $C(T) = C$ and λ be constant. Further, let the power be given by a step function. Therefore, Eq. (5) becomes

$$P(t) = C\frac{dT}{dt}(t) + \lambda\int_{u=0}^{t}\frac{dT}{du}(u)\frac{du}{\sqrt{t-u}}, \qquad t \geq 0 \tag{6a}$$

where

$$P(t) = P_0[H(t) - H(t - t_{\text{off}})] \tag{6b}$$

Here, t_{off} is the time at which the power is turned off. This mathematical model uses a single temperature (basically we let $T = T_{\text{BULK}} = T_{\text{TF}}$). The Heaviside step function is denoted by $H(t - t_0)$. The step-function behavior is introduced into the power ansatz for a particular reason, as will be demonstrated. The exact solution of Eq. (6) subject to the initial condition $T(0) = T_0$ is

$$T(t) - T_0 = \frac{P_0}{CA^2}\left\{\begin{array}{l}\left[\left(\frac{2A\sqrt{t}}{\sqrt{\pi}} - 1\right) + e^{A^2 t}\text{erfc}(A\sqrt{t})\right]H(t) \\ -\left[\left(\frac{2A\sqrt{t-t_{\text{off}}}}{\sqrt{\pi}} - 1\right) + e^{A^2(t-t_{\text{off}})}\text{erfc}(A\sqrt{t-t_{\text{off}}})\right]H(t-t_{\text{off}})\end{array}\right\}, \qquad t > 0 \tag{7}$$

where $A = (\lambda\sqrt{\pi}/C)$. To introduce a sensitivity analysis, notation needs to be extended for parameter differentiation; therefore, let $T(t) = T(t; C, \lambda)$. Taking the partial derivatives of T with respect to the two parameters C and λ produces the sensitivity coefficients. Doing so leads to the sensitivity functions

$$Z_C = \frac{\partial T}{\partial C}(t; C, \lambda) \quad \text{and} \quad Z_\lambda = \frac{\partial T}{\partial \lambda}(t; C, \lambda) \tag{8}$$

or, in terms of the modified sensitivity functions,

$$\Psi_C = C\frac{\partial T}{\partial C}(t; C, \lambda) \quad \text{and} \quad \Psi_\lambda = \lambda\frac{\partial T}{\partial \lambda}(t; C, \lambda) \tag{9}$$

The values of C and λ are formed based on the material properties of AlN [49] and MICROSIL [44]. These assigned values are indicated in Fig. 11. Table 2 presents all necessary data for the simulations. Preciseness of these parameters is not required for this illustration, but they are representative. Figure 11 displays the important and notable characteristics. Using a short time span, say $t < t_{\text{off}}$, to determine the coefficients C and λ, by a linear least-squares approach, may produce a suspect result for λ because little sensitivity exists in this time span. As graphically shown, using a 40 s time span allows for the sensitivity coefficient of λ to increase and the sensitivity coefficient of C to decrease.

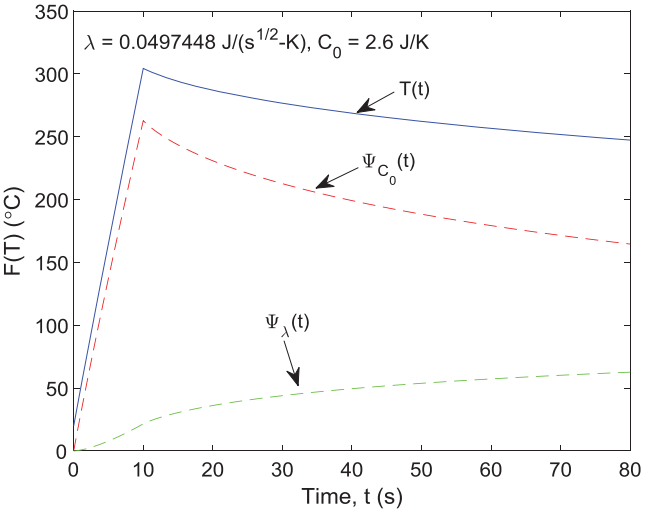

Fig. 11 Absolute modified sensitivity coefficients as a function of time.

2. *Sensitivity Analysis: Temperature-Dependent Properties*

Next, we examine a temperature dependency in $C(T)$ but restrict the model to a quadratic in temperature. With this assumption, Eq. (5) becomes

$$P(t) = C(T)\frac{dT}{dt}(t) + \lambda\int_{u=0}^{t}\frac{dT}{du}(u)\frac{du}{\sqrt{t-u}}, \qquad t \geq 0 \tag{10a}$$

$$P(t) = P_0[H(t) - H(t - t_{\text{off}})] \tag{10b}$$

where $C(T) = C_0 + C_1 T + C_2 T^2$. Again, this mathematical model uses a single temperature (basically we let $T = T_{\text{BULK}} = T_{\text{TF}}$). In this case, an analytic solution is most likely impossible to develop, owing to the nonlinear form of the integral equation involving both dT/dt and $T(t)$. However, we can numerically solve for $T(t)$ by a simple numerical method as now described. Let

$$\theta(t) = \frac{dT}{dt}(t) \tag{11a}$$

Table 2 Data for simulation

Item	Value
Insulation density ρ_{INS}	239 kg/m^3
Insulation thermal conductivity k_{INS}	0.025 W/(m · K)
Insulation specific heat $c_{p,\text{INS}}$	800 J/(kg · K)
Heater mass m_H	0.0026 kg
Heater specific heat $c_{p,H}$	1000 J/(kg · K)
Heater surface area A_t	0.0013 m^2
Current I	2 A
Resistance R	20 Ω
Power P	I^2 R W
Power magnitude P_0	80 W
Pulse duration t_{off}	10 s
Maximum experimental time t_{max}	80 s
Initial temperature T_0	293.15 K

Therefore,

$$P(t) = C(T)\theta(t) + \lambda \int_{u=0}^{t} \theta(u) \frac{du}{\sqrt{t-u}}, \qquad t > 0 \tag{11b}$$

where

$$T(t) = T_0 + \int_{u=0}^{t} \theta(u)\, du, \qquad t \geq 0$$

The evaluation of properties is performed based on one-time step lag, and using a product rectangular integration rule [16] leads to

$$\theta_i = \frac{P(t_i) - 2\lambda \sum_{j=1}^{i-1} \theta_j \left(\sqrt{t_i - t_{j-1}} - \sqrt{t_i - t_j} \right)}{C(T_{i-1}) + 2\lambda \sqrt{\Delta t}} \tag{11c}$$

and recovery of the temperature is obtained through the product rectangular rule, namely [16]

$$T_i = T_0 + \Delta t \sum_{j=1}^{i} \theta_j, \qquad i = 1, 2, \ldots, M \tag{11d}$$

The sensitivity coefficients for $\{C_0, C_1, C_2, \lambda\}$ can be determined by deriving integral equations for this system. To do so, again, we let $T(t) = T(t; C_0, C_1, C_2, \lambda)$ and implement parameter differentiation, based on taking the partial derivative with respect to each parameter C_0, C_1, C_2, and λ [51] in Eq. (10a), to form

$$-\frac{\partial T}{\partial t} = C(T)\frac{\partial Z_{C_0}}{\partial t} + \frac{\partial T}{\partial t}(C_1 + 2C_2T)Z_{C_0} + \lambda \int_{u=0}^{t} \frac{\partial Z_{C_o}}{\partial u} \frac{du}{\sqrt{t-u}},$$
$$t \geq 0, Z_{C_0} = Z_{C_0}(t_0; C_0, C_1, C_2, \lambda) \tag{12a}$$

$$-T\frac{\partial T}{\partial t} = C(T)\frac{\partial Z_{C_1}}{\partial t} + \frac{\partial T}{\partial t}(C_1 + 2C_2T)Z_{C_1} + \lambda \int_{u=0}^{t} \frac{\partial Z_{C_1}}{\partial u} \frac{du}{\sqrt{t-u}},$$
$$t \geq 0, Z_{C_1} = Z_{C_1}(t_0; C_0, C_1, C_2, \lambda) \tag{12b}$$

$$-T^2\frac{\partial T}{\partial t} = C(T)\frac{\partial Z_{C_2}}{\partial t} + \frac{\partial T}{\partial t}(C_1 + 2C_2T)Z_{C_2} + \lambda \int_{u=0}^{t} \frac{\partial Z_{C_2}}{\partial u} \frac{du}{\sqrt{t-u}},$$
$$t \geq 0, Z_{C_2} = Z_{C_2}(t_0; C_0, C_1, C_2, \lambda) \tag{12c}$$

$$-\int_{u=0}^{t} \frac{\partial T}{\partial u} \frac{du}{\sqrt{t-u}} = C(T)\frac{\partial Z_\lambda}{\partial t} + \frac{\partial T}{\partial t}(C_1 + 2C_2T)Z_\lambda$$
$$+ \lambda \int_{u=0}^{t} \frac{\partial Z_\lambda}{\partial u} \frac{du}{\sqrt{t-u}}, \quad t \geq 0, Z_\lambda = Z_\lambda(t_0; C_0, C_1, C_2, \lambda) \tag{12d}$$

The initial conditions for all sensitivity functions are analytically demonstrated to be zero based on $T(0; C_0, C_1, C_2, \lambda) = T(0) = T_0$. Equations (12a–12d) are solved independently once T is known. As before, nominal values based on AlN [52] and MICROSIL [44] are used in the simulation. Figure 12 displays the resulting absolute, modified sensitivity coefficients Ψ. The computational procedure, to obtain the numerical solution for these plots, is similar to the discretization described in Eq. (11c). At this junction, it is important to note the behavior of both Ψ_{C_1} and Ψ_λ. Here, Ψ_{C_1} has the highest, absolute modified sensitivity function. This will actually be indicated when reviewing the experimental results in a following section. To recover a representative value of λ, sufficient time is required when a pulsed power is applied.

3. *Linear, Least-Squares Method for Parameter Estimation*

With this analytic insight, a step pulse of current or voltage will be applied because the present system is not designed for maintaining a constant power pulse (no feedback loop at the present time). A constant current pulse renders an increasing power, whereas a constant voltage pulse produces a decreasing power with time during the activation periods. This is due to the heater's electrical resistance, as shown in Fig. 6. However, the "pulse" shape is representative and

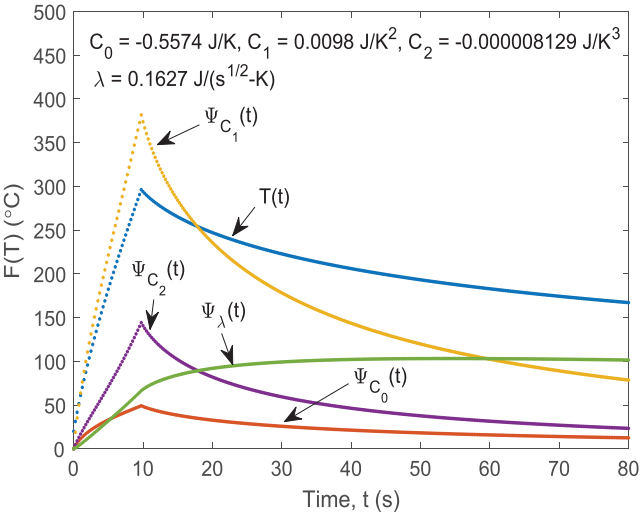

Fig. 12 Absolute modified sensitivity coefficients as a function of time.

key to the discussion. The determination of the heat capacitance function, $C(T)$, and λ is based on using a constant current pulse and tested over various currents. The present mathematical formulation is explicitly described as

$$P_m(t) = C(T_m)\frac{dT_m}{dt}(t) + \lambda \int_{u=0}^{t} \frac{dT_m}{du}(u) \frac{du}{\sqrt{t-u}}, \quad t \geq 0 \tag{13a}$$

$$C(T_m) = C_0 + C_1 T_m(t) + C_2 T_m^2(t) \tag{13b}$$

where $t = t_i$, $i = 1, 2, \ldots, M$ when discrete data are involved. As will be validated later, a single temperature is used based on the thin-film thermocouple located on the pin side of the heater (basically we let $T = T_{\text{BULK}} = T_{\text{TF}}$). To experimentally obtain these building block parameters, a parameter-estimation problem is proposed whereby the residual equation is defined as

$$r(t_i) = -P_m(t_i) + C(T_m(t_i))\frac{dT_m}{dt}(t_i) + \lambda \int_{u=0}^{t_i} \frac{dT_m}{du}(u) \frac{du}{\sqrt{t_i - u}},$$
$$i = 1, 2, \ldots, M \tag{14a}$$

The sum square of the residuals become

$$\overline{R}(\{C_0, C_1, C_2, \lambda\}) = \sum_{i=1}^{M} r^2(t_i)$$
$$= \sum_{i=1}^{M} \left(-P_m(t_i) + C(T_m(t_i))\frac{dT_m}{dt}(t_i) + \lambda \int_{u=0}^{t_i} \frac{dT_m}{du}(u) \frac{du}{\sqrt{t_i - u}} \right)^2 \tag{14b}$$

where the objective involves minimizing $\overline{R}$ with respect to each parameter to form a closed, linear system involving four algebraic equations. The four parameters are then solved for by matrix manipulation.

Figures 13a–13d display input and measurements required by the least-squares problem for estimating the four parameters. The RTD converted temperatures are indicated in this case as the temperature and current are low and the RTDs are stable. It is important to observe that the RTDs are producing highly favorable results, indicating that if the current leakage to the RTDs can be controlled then this heater produces a novel well-suited design for further investigation. Figure 13d sufficiently validates letting $T = T_{\text{BULK}} = T_{\text{TF}}$ until higher reliability of the RTDs is established.

Table 3 presents a sequential time investigation viewing the parameter sensitivity to the time span of the data collection set for the quadratic $C(T)$. Note that C_1 displays the least variation among the C coefficients and is least sensitive to the data time span. The behavioral results, shown in Table 3 for C_1, are then as expected. Table 4 renders results based on a cubic expansion for the heat capacitance $C(T)$. A similar sequential time study produces an indication of sufficient

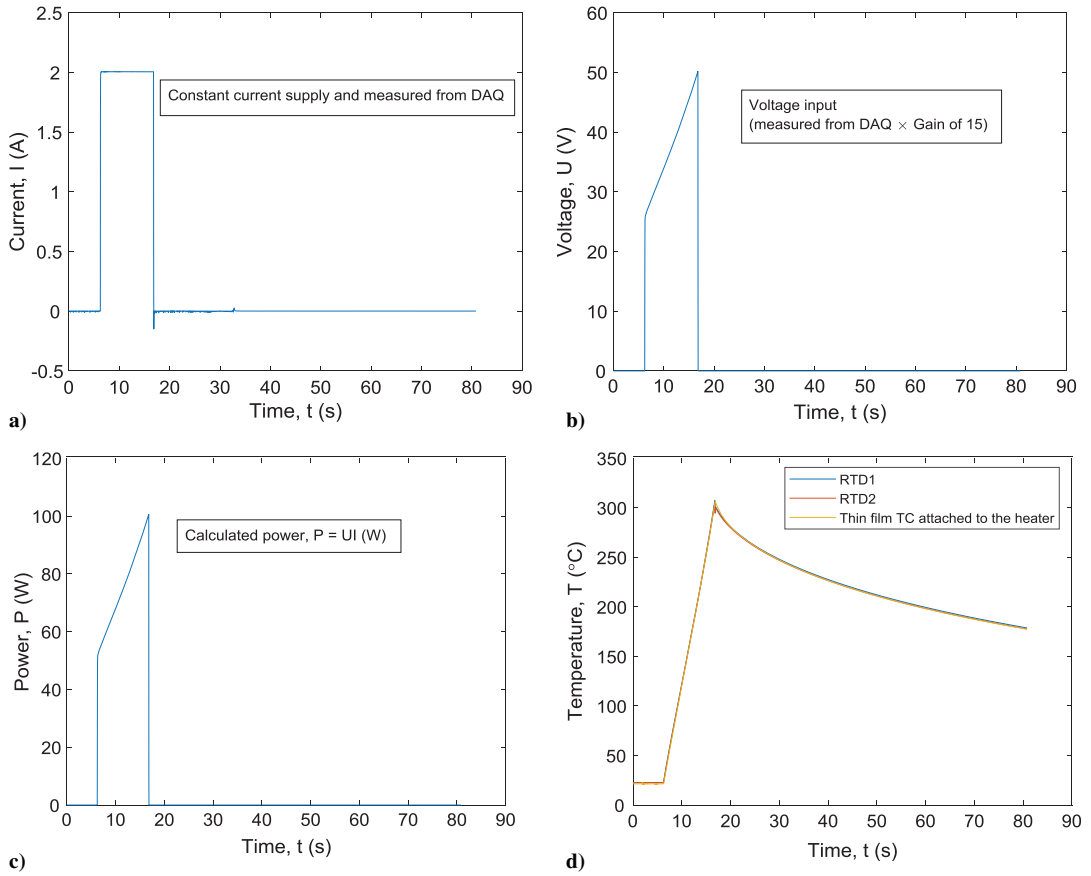

Fig. 13 Parameter estimation: a) input current pulse, b) input voltage $U(t)$, c) power calculation $P = UI$, and d) measured temperatures.

data. Figures 14a and 14b display the two reconstructed heat capacitances $C(T)$. A baseline curve is generated using data from Ref. [49] (with a measured heater mass based on $c_p(T)$ [48,49] with $m_H = 2.61 \times 10^{-3}$ kg) to provide a characteristic shape involving pure AlN. The inclusion of tungsten does not characteristically change this shape but will change the aggregate value. There is sufficient tungsten in the AlN heater to lower the aggregate magnitude over the reported temperature span but will not substantially change the trend. Observe that the cubic representation possesses an unexpected bend at high temperatures, which seems characteristically contradictive to expectations. This observation cannot normally be used because typically no baseline data are known. However, if we reconstruct the power based on Eq. (13a) and compare it to the measured power $P_m(t)$, then the choice of approximation becomes evident. Recovery of the power input for this extreme test case is highly favorable when the quadratic form of $C(T)$ is used as indicated in Figs. 15a and 15b. Power reconstruction near the jump conditions are well reconstructed when using the quadratic form of $C(T)$.

Table 3 Predictions based on quadratic $C(T)$ and constant λ

T-span, s	C_0, J/K	C_1, J/K^2	C_2, J/K^3	λ, J/(K · s$^{0.5}$)
$0.4t_{\max}$	−1.0358	0.0123	-1.1247×10^{-5}	0.1592
$0.6t_{\max}$	−1.0733	0.0125	-1.1458×10^{-5}	0.1581
$0.8t_{\max}$	−1.0212	0.0122	-1.1177×10^{-5}	0.1586
$t_{\max}$	−0.9543	0.0119	-1.0808×10^{-5}	0.1593

Table 4 Predictions based on cubic $C(T)$ and constant λ

T-span, s	C_0, J/K	C_1, J/K^2	C_2, J/K^3	C_3, J/K^4	λ, J/(K · s$^{0.5}$)
$0.4t_{\max}$	4.3285	−0.0262	7.8466×10^{-5}	-6.8255×10^{-8}	0.1586
$0.6t_{\max}$	4.3040	−0.0260	7.8267×10^{-5}	-6.8190×10^{-8}	0.1578
$0.8t_{\max}$	4.1473	−0.0248	7.4992×10^{-5}	-6.5461×10^{-8}	0.1584
$t_{\max}$	4.0841	−0.0242	7.3169×10^{-5}	-6.3786×10^{-8}	0.1592

The quadratic form of $C(T)$ and λ are described by

$$C(T) = -0.9543 + 0.0119T - 1.0808 \times 10^{-5}T^2 \ \text{(J/K)} \quad (15a)$$

$$\lambda = 0.1593 \ \text{(J/K}-\sqrt{\text{s}}\text{)} \quad (15b)$$

whereas the cubic form is determined as

$$C(T) = 4.0841\text{–}0.0242T + 7.3169 \times 10^{-5}T^2 - 6.3786 \times 10^{-8}T^3 \ \text{(J/K)} \quad (15c)$$

$$\lambda = 0.1592 \ \text{(J/K}-\sqrt{\text{s}}\text{)} \quad (15d)$$

The power distribution recovery for other test cases will use Eqs. (15a) and (15b). The first test case is described in Figs. 16a–16d based on a Gauss-shaped voltage applied to the heater, namely,

$$U(t) = U_0 \exp\left(-\frac{(t-\mu)^2}{\sigma^2}\right) \ \text{(V)} \quad (16)$$

where $U_0 = 52$ V, $\mu = 22$ s, $\sigma = 4$ s, and sampled at 48 Hz.

Figure 17a displays each energy-rate component described in Eq. (13a) as a function of time. The standard deviation (SD) in the power reconstruction is 1.55 W. The thin-film thermocouple sensor is highly sensitive to environmental vibration, and care should be taken. However, for this example, the local, large time jumps caused by this "table bump" are not significant to the illustration of accuracy in the power reconstruction. Figure 17b plots the measured power $P_m(t)$ and predicted power $P(t)$ for this model equation. The temperature data used to construct the time derivative of temperature are unfiltered (raw). A central difference is used for all interior values, backward

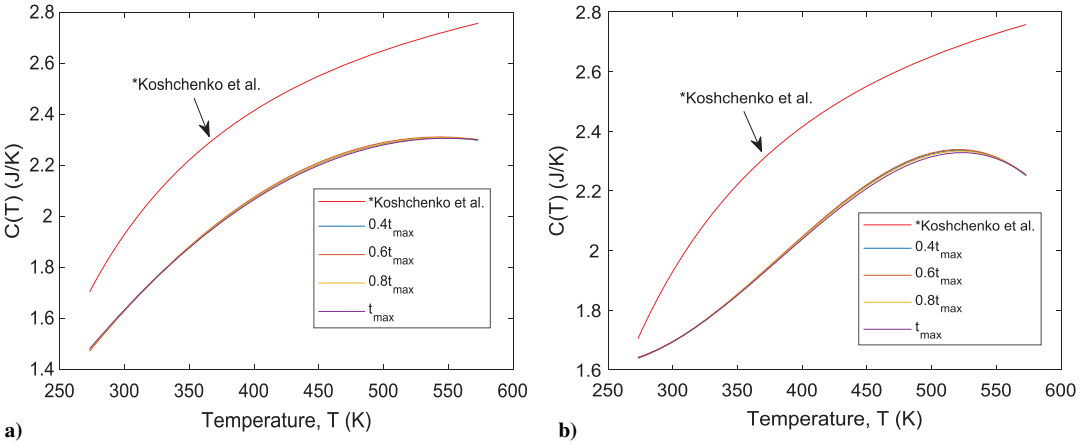

Fig. 14 Least-squares results: a) quadratic form, condition number $= 4.7 \times 10^{13}$, and b) cubic form, condition number $= 3.9 \times 10^{20}$.

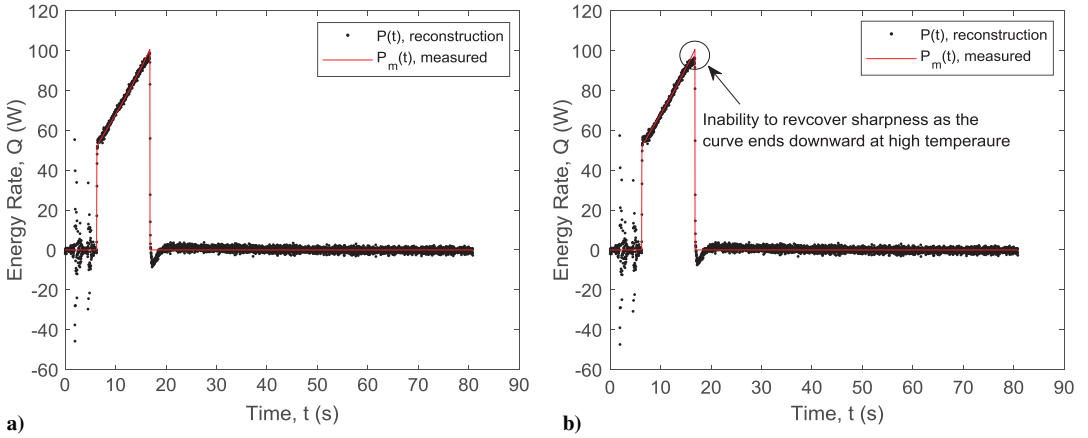

Fig. 15 Power: a) reconstructed power using quadratic $C(T)$ and λ, and b) reconstructed power using cubic form for $C(T)$ and λ.

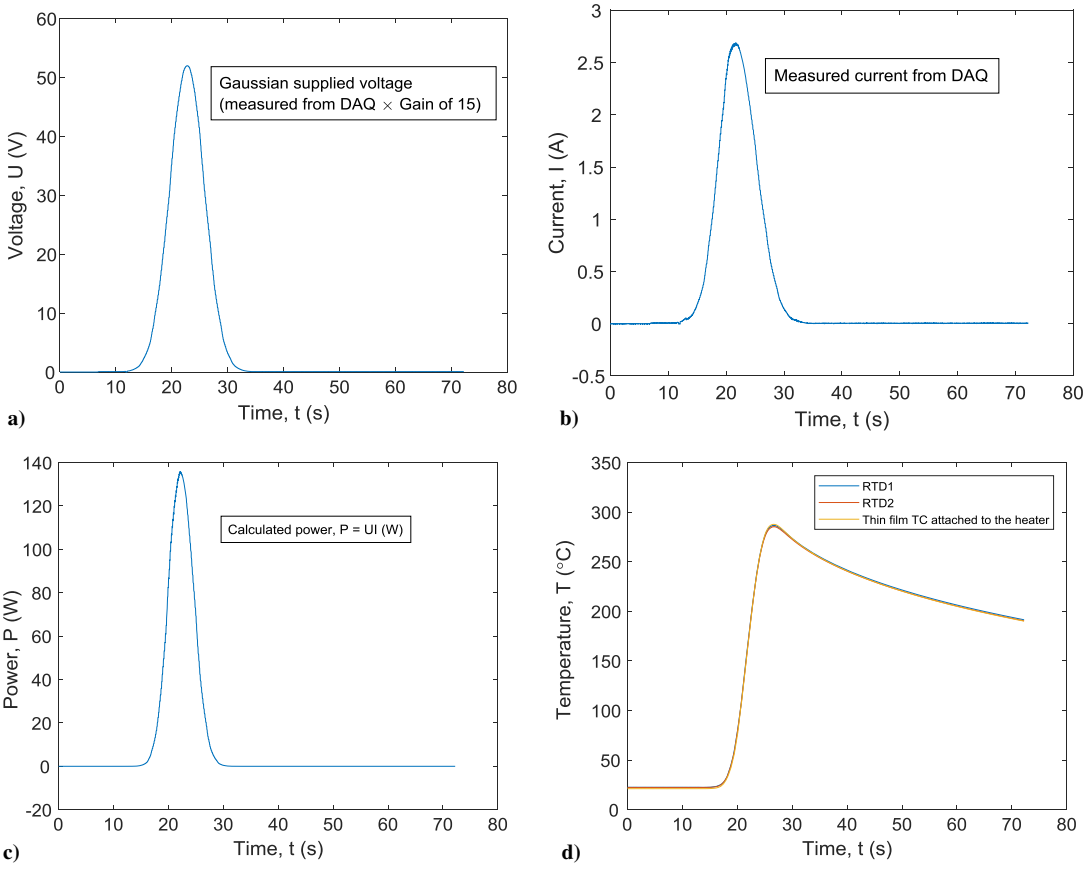

Fig. 16 Data: a) input Gauss voltage (DAQ), b) measured current, c) power calculation $P = UI$, and d) measured temperatures.

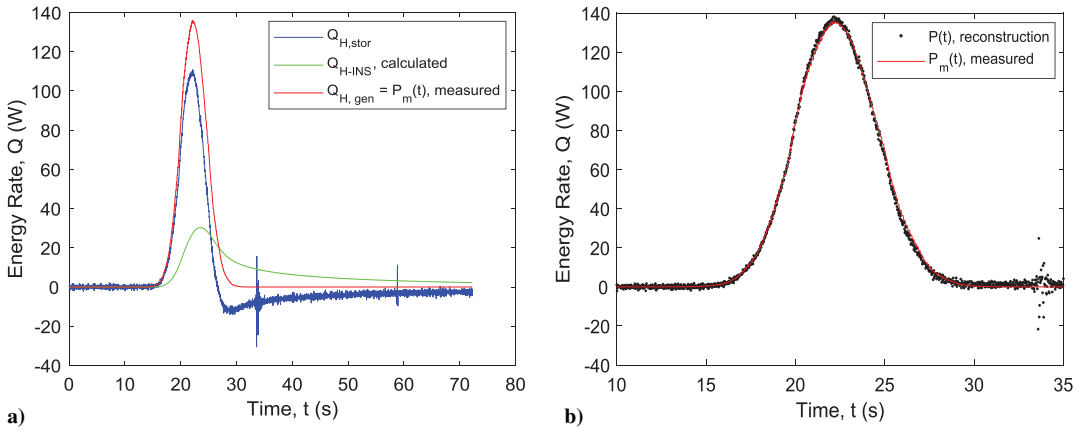

Fig. 17 Results: a) energy rate for individual components in Eq. (13a), and b) comparison between reconstructed and measured power.

difference for the first point, and forward difference for the last point. The assumption of good thermal contact between the heater and the insulation can be visually validated with the aid of the power reconstruction as displayed in Fig. 17b.

A second more challenging test to the previous case is now presented. In this case, the voltage input is given by the double Gauss function:

$$U(t) = U_{01}\exp\left(-\frac{(t-\mu_1)^2}{\sigma_1^2}\right) + U_{02}\exp\left(-\frac{(t-\mu_2)^2}{\sigma_2^2}\right)\ (\mathrm{V}) \quad (17)$$

where $U_{01} = 50$ V, $U_{02} = 25$ V, $\sigma_1 = 4$ s, $\sigma_2 = 3$ s, $\mu_1 = 15$ s, $\mu_2 = 25$ s at a sampling rate of 48 Hz. Figures 18a–18d display the input voltage (driven by LabView) as measured by the DAQ and the other building block components for this test as the power is reconstructed. Figure 19 displays the heating rate $\mathrm{d}T/\mathrm{d}t$ using raw data and the difference calculations previously noted. It is evident that a heating rate of approximately 49°C/s is generated in the heater based on the thin-film thermocouple. The individual RTDs are also used in this figure for defining a time derivative of the "bulk" temperature. That is, Ta2 involves the average of the thin film and RTD1, whereas Ta3 is calculated on the average of the thin film, RTD1 and RTD results. The RTDs are not contaminated with the spurious current. Additionally, the RTDs produce fast and seemingly reliable results. Figure 20a displays the input power $P_m(t)$ and reconstructed power $P(t)$. Graphically, they appear to produce favorable results. Figure 20b displays the difference between the two over the test time span. The difference near the peak is about 3%, which is relatively good, considering that the heating rate is about 49°C/s at that point. Again, the assumption of good thermal contact

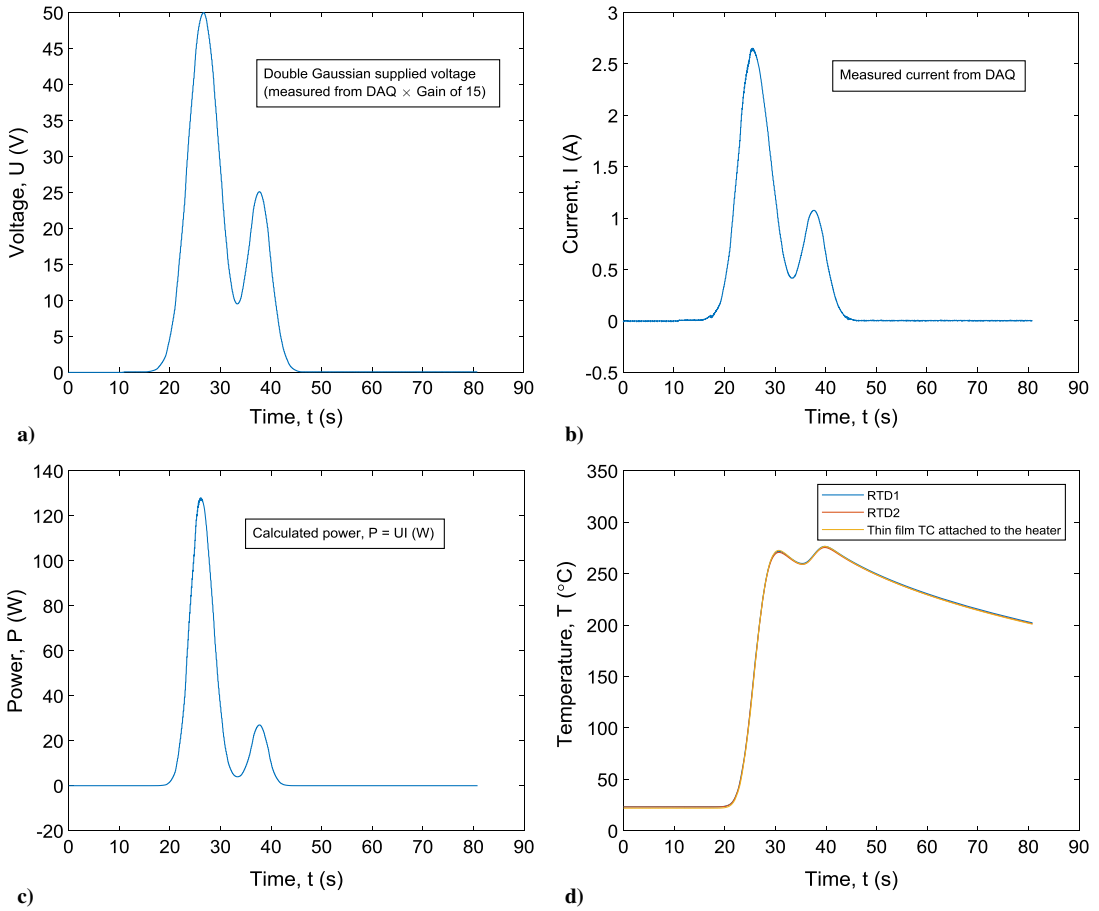

Fig. 18 Data: a) input double Gauss voltage, b) measured current, c) power calculation $P = UI$, and d) measured temperatures.

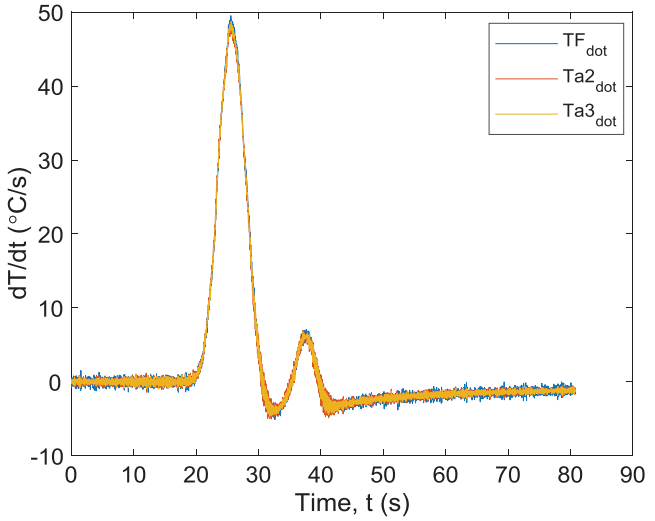

Fig. 19 Comparison of dT/dt by finite difference and averaging of RTDs, namely TF, Ta2 = (RTD1 + RTD2)/2, Ta3 = (TF + RTD1+ RTD2)/3.

between the heater and the insulation can be visually validated with the aid of the power reconstruction shown in Fig. 20a.

4. Modified Model Equation for Heat Flux Source

The model equation given in Eq. (13a) can now be adjusted to account for heat loss into a sample. In this case, a quantifiable heat flux source is now proposed. To demonstrate model accuracy, a test is devised using a copper (CA110, Speedy Metals) slug of measured dimensions 25.4 × 25.4 × 1.5875 mm with a thin-film thermocouple (OMEGA CO2-K) attached to the backside of the copper plate. The bead is carefully adhered to the copper with Graphi-Bond 669, while a thin shimmer of mica is placed between the thin-ribbon leads and

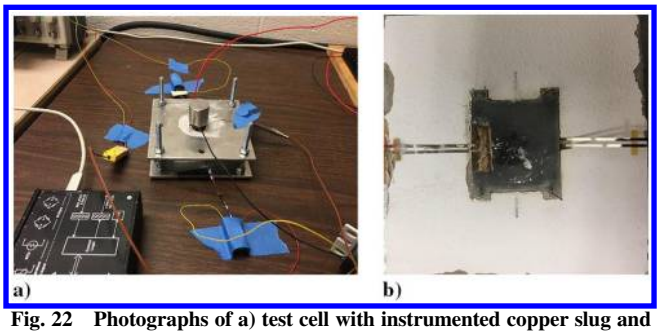

Fig. 22 Photographs of a) test cell with instrumented copper slug and heater, and b) ZIRCAR insulation with a milled pocket containing the copper slug and heater.

copper slug near its edge (about 1/4 in. in length) to assure electrical isolation and preventing a junction to be formed on the edge. A thin layer of AREMCO Heat-Away 641 silver paste is applied between the heater and copper slug. Though this paste is an electrical conductor, no current leakage to the copper or any sample from the heater has been observed. The next interfacial paste to be studied is an electrical insulator.

Figures 21a and 21b show the new configuration where the heat flux can now be evaluated and compared to the installed slug calorimeter. Figure 22a shows the actual containment cell where the bolts are hand-tightened to assure good contact without breaking the small fin connections in the heater. Figure 22b displays the ZIRCAR insulation with a milled pocket containing the copper slug and heater.

Equation (13a) is now modified to account for the heat loss into the copper. Doing so produces

$$P_m(t) = C(T_m)\frac{dT_m}{dt}(t) + \lambda\beta\int_{u=0}^{t}\frac{dT_m}{du}(u)\frac{du}{\sqrt{t-u}} + q''_{H,\text{out}}A_s, \quad t \geq 0 \tag{18}$$

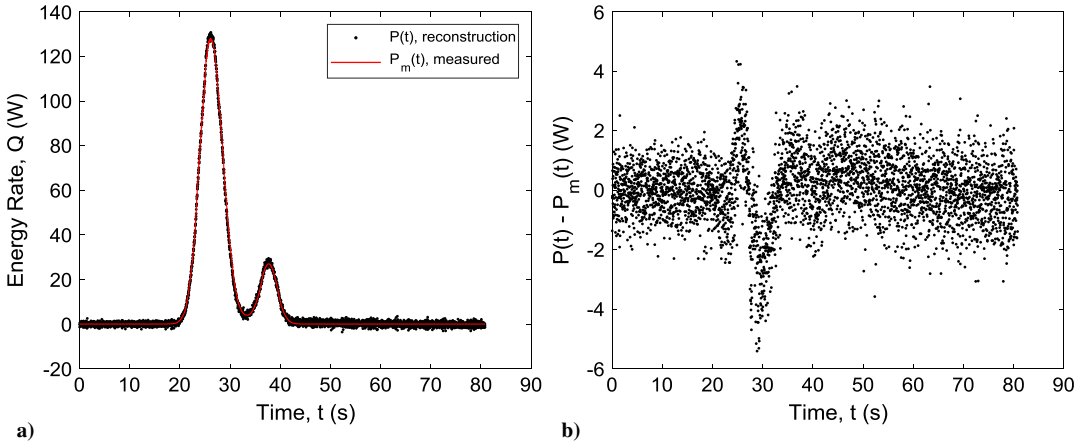

Fig. 20 Results: a) power reconstruction $P(t)$ and measured power $P_m(t)$, and b) difference between the reconstructed and measured power.

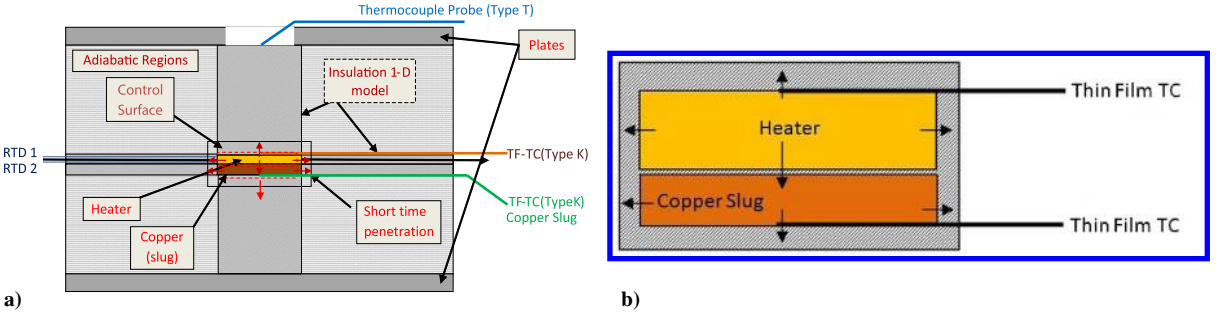

Fig. 21 Representations of a) schematic for heat flux evaluation, and b) zoomed-in view of copper–heater interface showing (arrows) heat flow directions.

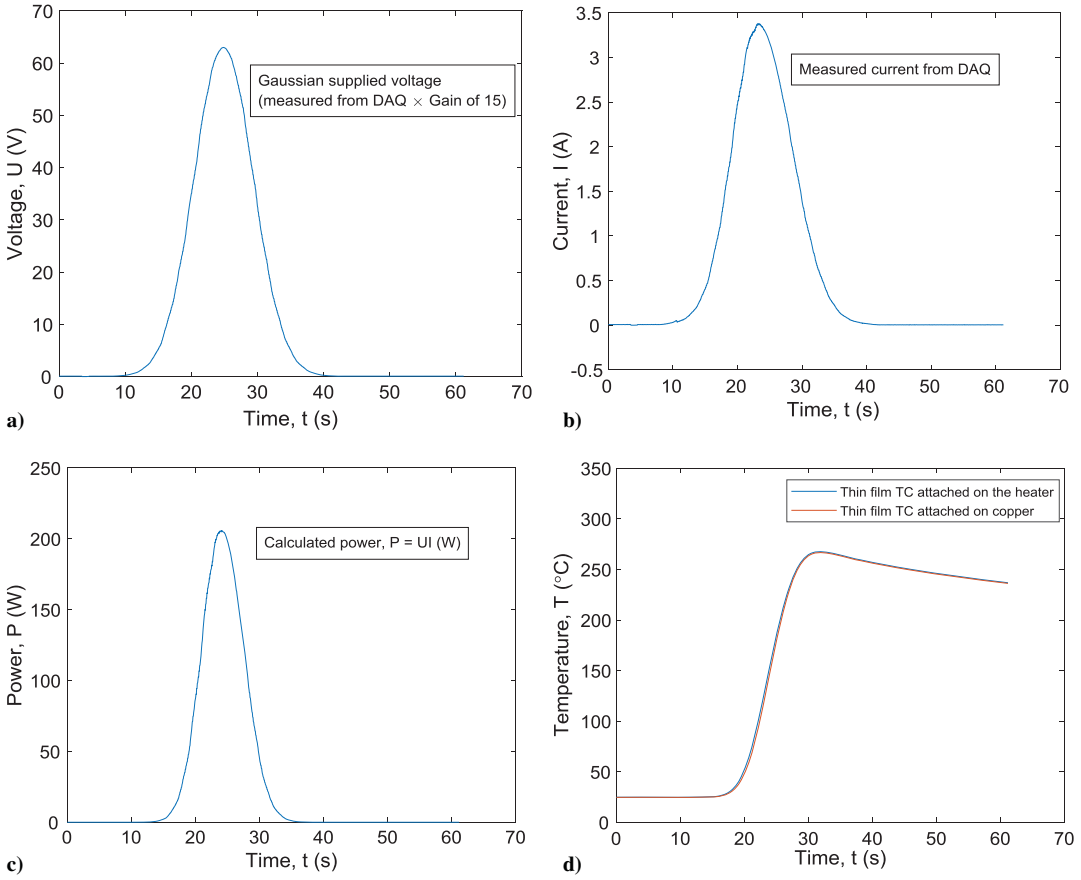

Fig. 23 Data: a) input single Gauss voltage, b) measured current, c) power calculation UI, and d) measured thin-film temperatures.

where $\beta = (A_t - A_s)/A_t$ Again, the present model leading to the presented plots assumes $T = T_{\text{TF}} = T_{\text{BULK}}$. Meanwhile, the copper slug energy balance leads to

$$q''_{\text{Cu,in}} A_s = C_{\text{Cu}}(T_{\text{Cu},m}) \frac{dT_{\text{Cu},m}}{dt}(t) + q''_{\text{Cu-INS}} \overline{A}_{\text{faces}}, \qquad t \geq 0 \tag{19a}$$

$$q''_{\text{Cu,in}} A_s = C_{\text{Cu}}(T_{\text{Cu},m}) \frac{dT_{\text{Cu},m}}{dt}(t) + (\lambda\overline{\beta})_{\text{INS}} \int_{u=0}^{t} \frac{dT_{\text{INS,Cu}}}{du}(u) \frac{du}{\sqrt{t-u}}, \quad t \geq 0 \tag{19b}$$

$$q''_{\text{Cu,in}} A_s = C_{\text{Cu}}(T_{\text{Cu},m}) \frac{dT_{\text{Cu},m}}{dt}(t) + (\lambda\overline{\beta})_{\text{INS}} \int_{u=0}^{t} \frac{dT_{\text{Cu},m}}{du}(u) \frac{du}{\sqrt{t-u}}, \quad t \geq 0 \tag{19c}$$

where β accounts for surface area changes in insulation contact for the heater model equation. Because an identical insulation is used about the copper, $\overline{\lambda}$ should be the same. Hence, we can introduce the geometric correction factor $\overline{\beta}$ for adjusting the wetted area in contact to the insulation in the copper model equation. Again, it is assumed that the slug is in perfect thermal contact with the insulation as MICROSIL is compliant. This assumption is used in Eqs. (19a–19c).

5. *Evaluation of Heat Flux by Slug Calorimeter*

The mass of the copper slug was measured using the Sartorius TE214S scale leading to $m_{\text{Cu}} = 9.166$ g The density of pure copper is $\rho_{\text{Cu}} = 8933$ kg/m^3 [53], whereas the temperature-dependent specific heat is given as $c_{p,\text{Cu}}(T) = 65.9(5.44 + 0.001462T)$ J/(kg · K) [54].

To initially verify the feasibility of the model used in conjunction with the AlN heater, the power is generated using a Gauss form of voltage. Figures 23a–23c present the building blocks for the power input, whereas Fig. 23d presents the resulting temperature history as generated by the thin-film thermocouple attached to the pin side of the heater. The voltage is given as

$$U(t) = U_0 \exp\left(-\frac{(t-\mu)^2}{\sigma^2}\right) \text{ (V)} \tag{20}$$

where $U_0 = 63$ V, $\mu = 20$ s, $\sigma = 6$ s and sampled at 19.2 Hz. Figure 23d indicates little difference in temperature between the back-side heater temperature (TF thermocouple) and copper slug temperature, indicating excellent interfacial contact.

Figure 24a presents the individual contributions of the model equations given in Eqs. (18) and (19). This reveals several important physical features in the energy balances. First, the storage of energy must be accounted for even in a thin heater of 1.02 mm thickness. Second, the insulation is clearly not perfect (not adiabatic) and should be accounted for. Third, the time response of the slug with the thin film on the back surface is sufficient. Figure 24b displays the type T thermocouple that estimates the backside temperature of the insulation.

Figures 25a and 25b display the reconstruction of the heat flux from the slug using Eq. (19c) and exiting heat flux reconstructed from Eq. (18). In Fig. 25a, the heat loss to the insulation about the copper slug is omitted, whereas Fig. 25b accounts for the heat loss to the modeled insulation in the copper slug.

A second power profile is proposed involving the double Gauss function for the voltage defined as

$$U(t) = U_{01} \exp\left(-\frac{(t-\mu_1)^2}{\sigma_1^2}\right) + U_{02} \exp\left(-\frac{(t-\mu_2)^2}{\sigma_2^2}\right) \text{ (V)} \tag{21}$$

with the parameters: $U_{01} = 60$ V, $U_{02} = 45$ V, $\sigma_1 = 4$ s, $\sigma_2 = 4$ s, $\mu_1 = 15$ s, $\mu_2 = 25$ s and sampled at 19.2 Hz. The arrangement of figures is identical to that displayed with the single Gauss voltage

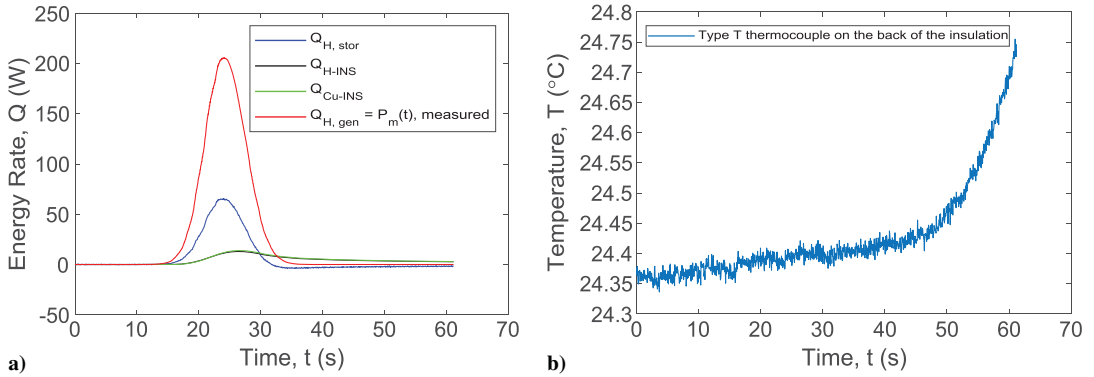

Fig. 24 Results: a) energy rate for individual components in Eqs. (18) and (19), and b) backside TC (shows penetration time).

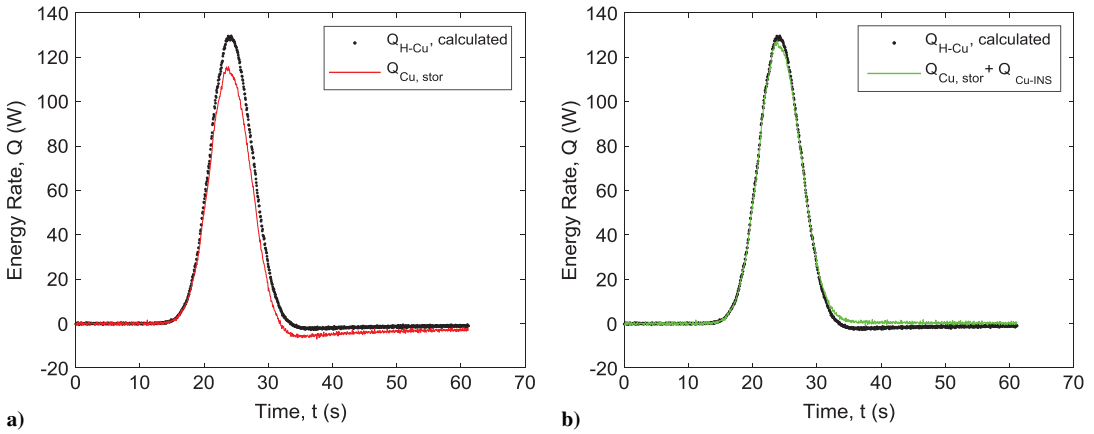

Fig. 25 Power reconstruction: a) insulation is assumed adiabatic, and b) insulation is assumed real.

function. Figures 26a–26d present the input data using the defined double Gauss voltage driver. Figure 27 displays the individual contributions of the energy rate terms in the energy balance associated with both the heater and copper calorimeter plate. Again, energy storage in this thin heater is significant. Figure 28a presents the estimated copper entering heat flux to that of the heater model exiting heat flux. Figure 28b displays the relative difference between the two heat flux estimates in the time span where the most rapid changes in temperature occur. The time rate of change of temperature dT/dt in the heater and copper is about 33°C/s, with a corresponding maximum heat flux about 21 W/cm^2. These preliminary results demonstrate excellent accuracy that lies within 3–5% of each other.

6. *Transient Uncertainty Propagation in Heater and Slug Calorimeter*

Uncertainty analysis [20,55–60] is a fundamental tool for understanding how the systematic and random errors propagate through the experimental process or system. The open literature has produced a healthy interest and response in this area. Several approaches have been proposed involving various levels of sophistication. For this preliminary study, uncorrelated data are assumed, and a type B (scientific judgment [55]) evaluation procedure is followed. Under these assumptions, a conventional engineering view involving the Kline–McClintock [59] formulation is basically produced. Each control volume (heater and slug) produces an uncertainty model based on the previously outlined assumptions. Clearly, components remain unknown, such as insufficient physics in the model, etc. However, for this preliminary investigation, the procedure is well defined based on the models for the heater and slug. The approach described in Ref. [20] is instituted for this initial investigation as a means for gathering a physical basis of understanding.

a. Uncertainty Analysis for the Oasis Heater Model. Equation (18) can be rewritten as

$$q''_{H,\text{out}}(t) = q''_{H,\text{out}}\left(t; P_m, C(T_m), \dot{T}_m, Q_{H-\text{INS}}, A_s\right) = \frac{1}{A_s}\left[P_m(t) - C(T_m)\frac{dT_m}{dt}(t) - Q_{H-\text{INS}}(t)\right] \tag{22a}$$

which explicitly indicates the functional dependency on the listed parameters. The energy loss from the heater to the insulation is

$$Q_{H-\text{INS}}(t) = \lambda\beta\int_{u=0}^{t}\frac{dT_m}{du}(u)\frac{du}{\sqrt{t-u}}, \qquad t \geq 0 \tag{22b}$$

and represents a collective quantity [20] involving $\lambda, \beta, (dT_m/dt)(t)$ from which an uncertainty estimate can be physically assigned. Taking partial derivative with respect to $\phi_1 = P_m$, $\phi_2 = C(T_m)$, $\phi_3 = \dot{T}_m$, $\phi_4 = Q_{H-\text{INS}}$, and $\phi_5 = A_s$ produces

$$\frac{\partial q''_{H,\text{out}}}{\partial P_m} = \frac{1}{A_s}, \quad \frac{\partial q''_{H,\text{out}}}{\partial C} = \frac{-\dot{T}_m(t)}{A_s}, \quad \frac{\partial q''_{H,\text{out}}}{\partial \dot{T}_m} = \frac{-C(T_m)}{A_s}, \quad \frac{\partial q''_{H,\text{out}}}{\partial Q_{H-\text{INS}}} = \frac{-1}{A_s}, \quad \frac{\partial q''_{H,\text{out}}}{\partial A_s} = \frac{-[P_m(t) - C(T_m)\dot{T}_m(t) - Q_{H-\text{INS}}(t)]}{A_s^2} \tag{23}$$

respectively. With these explicit expressions, each uncertainty term can be formed based on

$$\frac{\partial q''_{H,\text{out}}}{\partial \phi_l}\Delta\phi_l, \qquad l = 1, \ldots, 5 \tag{24a}$$

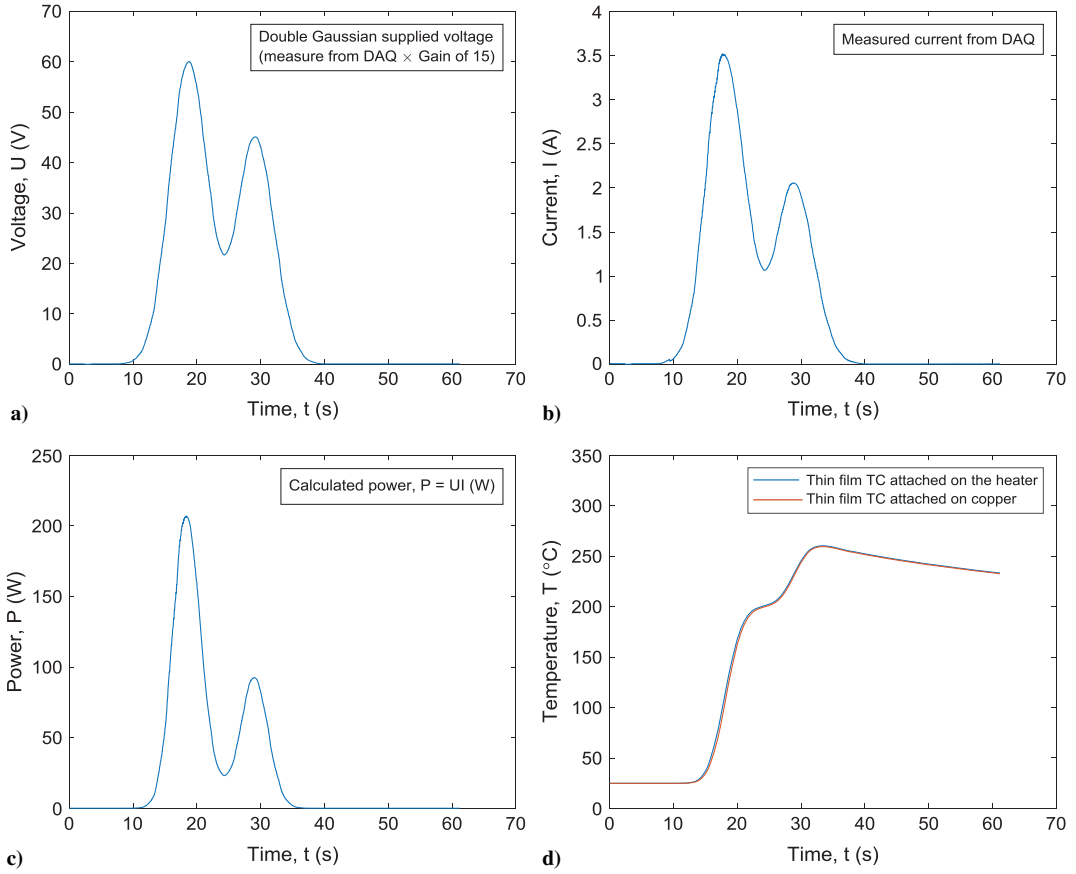

Fig. 26 Data: a) input double Gauss voltage, b) measured current, c) power calculation $P = UI$, and d) measured thin-film temperatures.

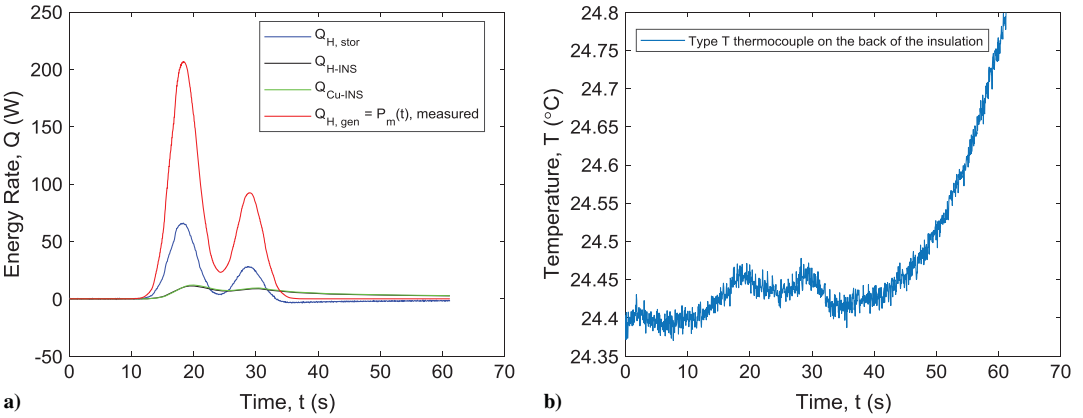

Fig. 27 Results: a) components of the energy balances (heater and copper slug), and b) backside TC (thermal penetration time).

and because a type B analysis [54] is assumed for the present study, Eq. (24a) can be alternatively expressed as

$$\frac{\partial q''_{H,\text{out}}}{\partial \phi_l}\Delta\phi_l = \left(\frac{\partial q''_{H,\text{out}}}{\partial \phi_l}\phi_l\right)\left\|\frac{\Delta\phi_l}{\phi_l}\right\|_\infty, \qquad l = 1, \ldots, 5 \tag{24b}$$

where $\|\Upsilon\|_\infty = \max|\Upsilon|$ is merely the infinity norm (max-norm) for defining the maximum relative uncertainty. The total uncertainty can be expressed in terms of root-sum-square method [58] as

$$\Delta q''_{H,\text{out}}\left(t; P_m, C(T_m), \dot{T}_m, Q_{H-\text{INS}}, A_s\right) = \sqrt{\sum_{l=1}^{5}\left[\left(\frac{\partial q''_{H,\text{out}}}{\partial \phi_l}\phi_l\right)\left\|\frac{\Delta\phi_l}{\phi_l}\right\|_\infty\right]^2}, \qquad t \geq 0 \tag{25}$$

Based on the open literature, experience, and calculations,

$$\left\|\frac{\Delta\phi_l}{\phi_l}\right\|_\infty, \qquad l = 1, \ldots, 5$$

are explicitly estimated as

$$\left\|\frac{\Delta P_m}{P_m}\right\|_\infty = 1\%, \quad \left\|\frac{\Delta C}{C}\right\|_\infty = 5\%, \quad \left\|\frac{\Delta \dot{T}_m}{\dot{T}_m}\right\|_\infty = 5\%,$$
$$\left\|\frac{\Delta Q_{H-\text{INS}}}{Q_{H-\text{INS}}}\right\|_\infty = 10\%, \quad \left\|\frac{\Delta A_s}{A_s}\right\|_\infty = 2\%$$

These values can be additionally perturbed but represent reasonable values for understanding the propagation of errors in the model displayed in Eq. (18). Figure 29 displays the temporal behavior of the component terms defined in Eq. (25). Figure 30

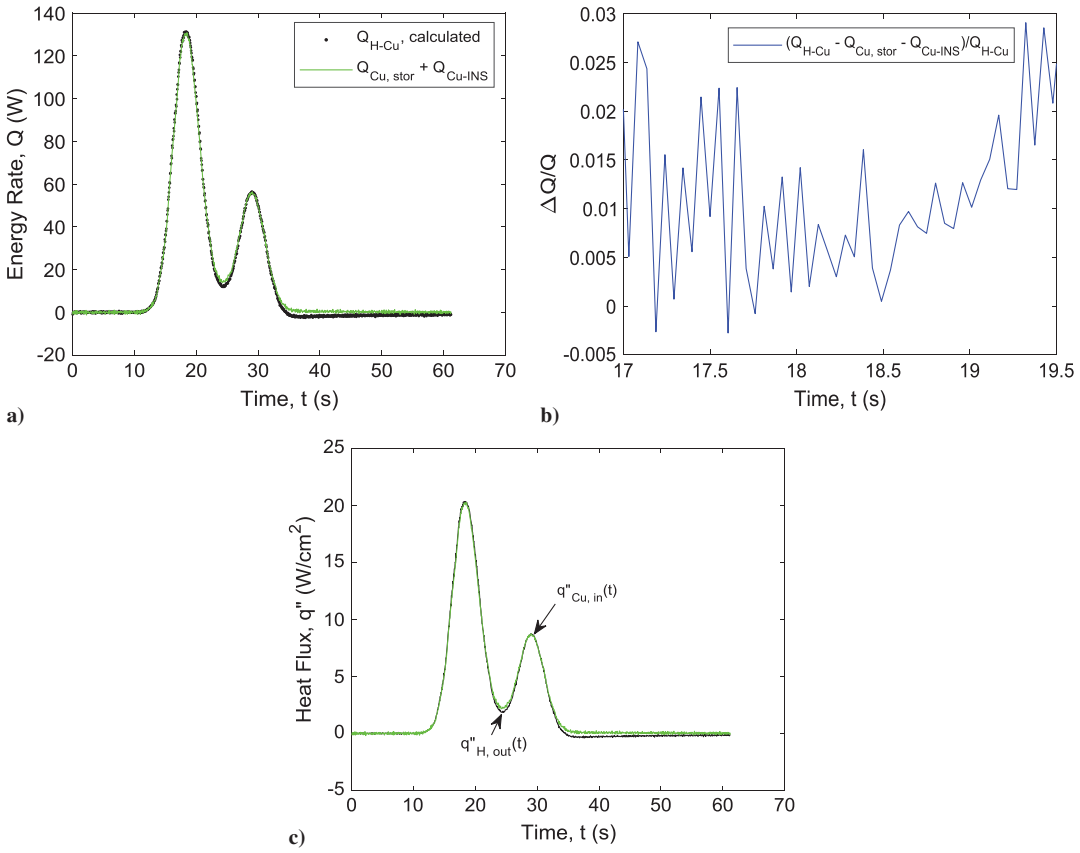

Fig. 28 Results: a) reconstructed energy rate predictions, b) relative difference (near high-interest time period), and c) comparison between $q''_{H,\text{out}}$ and $q''_{\text{Cu,in}}$.

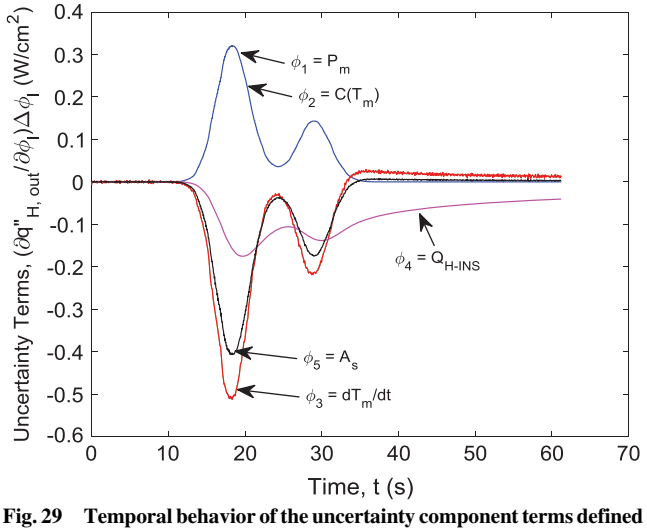

Fig. 29 Temporal behavior of the uncertainty component terms defined in Eq. (25).

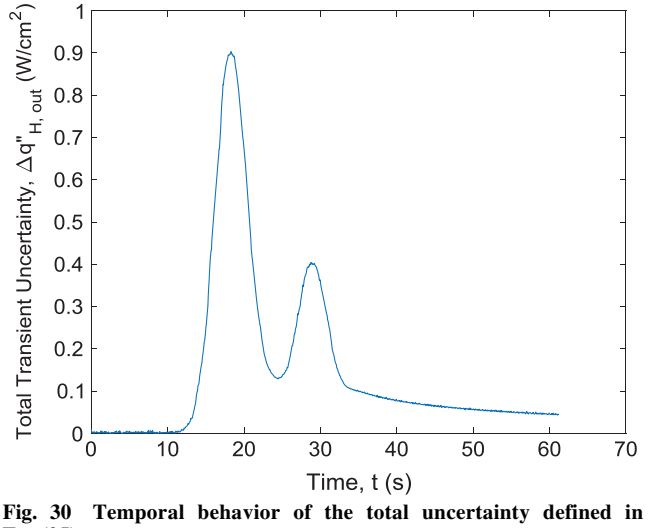

Fig. 30 Temporal behavior of the total uncertainty defined in Eq. (25).

shows the temporal behavior of the total uncertainty, $\Delta q''_{H,\text{out}}(t; P_m, C(T_m), \dot{T}_m, Q_{H-\text{INS}}, A_s)$. The peak total uncertainty value is less than 0.9 W/cm^2 at time $t \approx 18$ s. The heat flux at this time, from Fig. 28c, is approximately 20.8 W/cm^2, leading to a ratio of less than 5% for input estimates of the local uncertainties. Figure 31 presents the estimated heat flux with error bars (down sampled for visual clarity) as generated by $q''_{H,\text{out}} \pm \Delta q''_{H,\text{out}}$.

b. Uncertainty Analysis for the Copper Slug Model. Equation (19a) can be rewritten as

$$q''_{\text{Cu,in}}(t) = q''_{\text{Cu,in}}(t; C_{\text{Cu}}(T_{\text{Cu},m}), \dot{T}_{\text{Cu},m}, Q_{\text{Cu-INS}}, A_s) = \frac{1}{A_s}\left[C_{\text{Cu}}(T_{\text{Cu},m})\frac{dT_{\text{Cu},m}}{dt}(t) + Q_{\text{Cu-INS}}(t)\right], \quad t \geq 0 \qquad (26a)$$

which explicitly indicates the functional dependency on the listed parameters. The collective term

$$Q_{\text{Cu-INS}}(t) = (\lambda\overline{\beta})_{\text{INS}} \int_{u=0}^{t} \frac{dT_{\text{Cu},m}}{du}(u)\frac{du}{\sqrt{t-u}}, \qquad t \geq 0 \qquad (26b)$$

is the energy loss from the copper slug to the insulation, and it is a quantity to which an uncertainty can be estimated and assigned. Taking partial derivative with respect to $\Phi_1 = C_{\text{cu}}(T_{\text{Cu},m})$, $\Phi_2 = \dot{T}_{\text{Cu},m}$, $\Phi_3 = Q_{\text{Cu-INS}}$, and $\Phi_4 = A_s$ produces

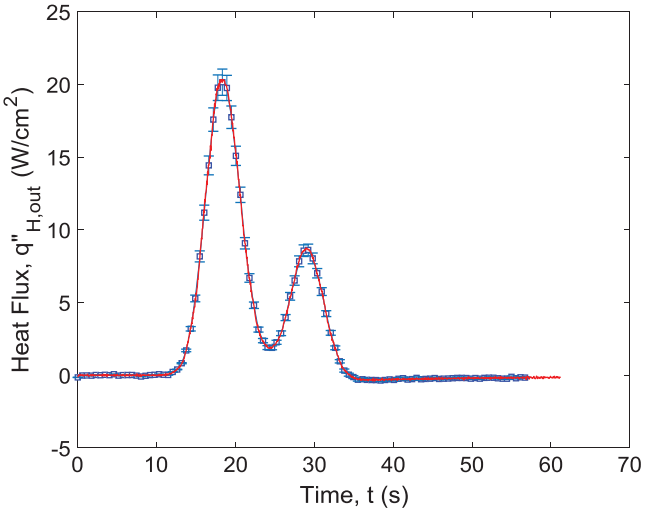

Fig. 31 Estimated outgoing heater heat flux with uncertainty bars.

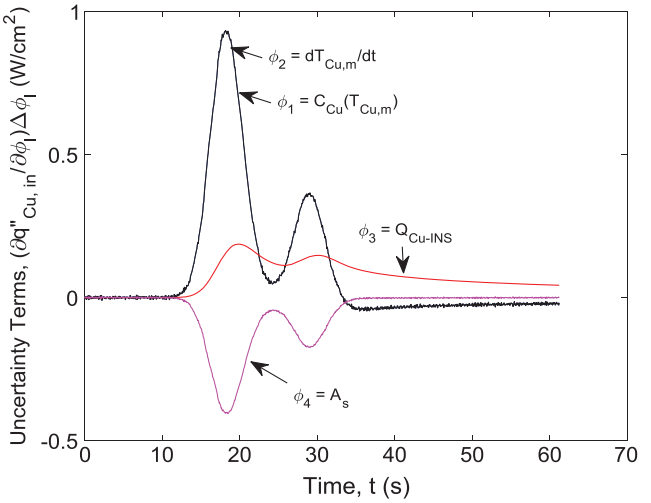

Fig. 32 Temporal behavior of the uncertainty component terms defined in Eq. (28b).

$$\frac{\partial q''_{\mathrm{Cu,in}}}{\partial C_{\mathrm{Cu}}} = \frac{\dot{T}_{\mathrm{Cu},m}(t)}{A_s}, \quad \frac{\partial q''_{\mathrm{Cu,in}}}{\partial \dot{T}_{\mathrm{Cu},m}} = \frac{C_{\mathrm{Cu}}(T_{\mathrm{Cu},m})}{A_s}, \quad \frac{\partial q''_{\mathrm{Cu,in}}}{\partial Q_{\mathrm{Cu-INS}}} = \frac{1}{A_s}$$
$$\frac{\partial q''_{\mathrm{Cu,in}}}{\partial A_s} = \frac{-[C_{\mathrm{Cu}}(T_{\mathrm{Cu},m})\dot{T}_{\mathrm{Cu},m}(t) + Q_{\mathrm{Cu-INS}}(t)]}{A_s^2} \tag{27}$$

respectively. With these explicit expressions, each uncertainty term can be formed based on

$$\frac{\partial q''_{\mathrm{Cu,in}}}{\partial \Phi_l}\Delta\Phi_l, \qquad l = 1, \ldots, 4 \tag{28a}$$

and because a type B analysis is assumed for the present study, Eq. (28a) can be alternatively expressed as

$$\frac{\partial q''_{\mathrm{Cu,in}}}{\partial \Phi_l}\Delta\Phi_l = \left(\frac{\partial q''_{H,\mathrm{out}}}{\partial \Phi_l}\Phi_l\right)\left\|\frac{\Delta\Phi_l}{\Phi_l}\right\|_\infty, \qquad l = 1, \ldots, 4 \tag{28b}$$

The total uncertainty can be expressed in terms of root-sum-square method [58] as

$$\Delta q''_{\mathrm{Cu,in}}(t; C_{\mathrm{Cu}}(T_{\mathrm{Cu},m}), \dot{T}_{\mathrm{Cu},m}, Q_{\mathrm{Cu-INS}}, A_s) = \sqrt{\sum_{l=1}^{4}\left[\left(\frac{\partial q''_{\mathrm{Cu,in}}}{\partial \Phi_l}\Phi_l\right)\left\|\frac{\Delta\Phi_l}{\Phi_l}\right\|_\infty\right]^2} \tag{29}$$

Based on the open literature, experience, and calculations

$$\left\|\frac{\Delta\Phi_l}{\Phi_l}\right\|_\infty, \qquad l = 1, \ldots, 4$$

can be explicitly estimated as

$$\left\|\frac{\Delta C_{\mathrm{Cu}}}{C_{\mathrm{Cu}}}\right\|_\infty = 5\%, \qquad \left\|\frac{\Delta \dot{T}_{\mathrm{Cu},m}}{\dot{T}_{\mathrm{Cu},m}}\right\|_\infty = 5\%,$$
$$\left\|\frac{\Delta Q_{\mathrm{Cu-INS}}}{Q_{\mathrm{Cu-INS}}}\right\|_\infty = 10\%, \qquad \left\|\frac{\Delta A_s}{A_s}\right\|_\infty = 2\%$$

Figure 32 displays the temporal behavior of the component terms defined in Eq. (28b). Figure 33 shows the temporal behavior of the total uncertainty $\Delta q''_{\mathrm{Cu,in}}(t; C_{\mathrm{Cu}}(T_{\mathrm{Cu},m}), \dot{T}_{\mathrm{Cu},m}, Q_{\mathrm{Cu-INS}}, A_s)$. The peak total uncertainty value is less than 1.4 W/cm^2 at time $t \approx 18$ s. The heat flux at this time, from Fig. 28c, is approximately

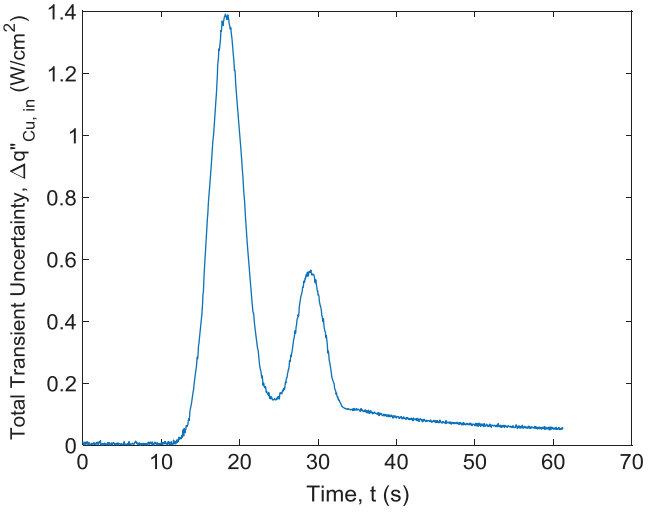

Fig. 33 Temporal behavior of the total uncertainty defined in Eq. (29).

20.8 W/cm^2, leading to ratio of less than 7% for input estimates of the local uncertainties. Figure 34 presents the predicted slug heat flux with error bars based on the presented uncertainty analysis.

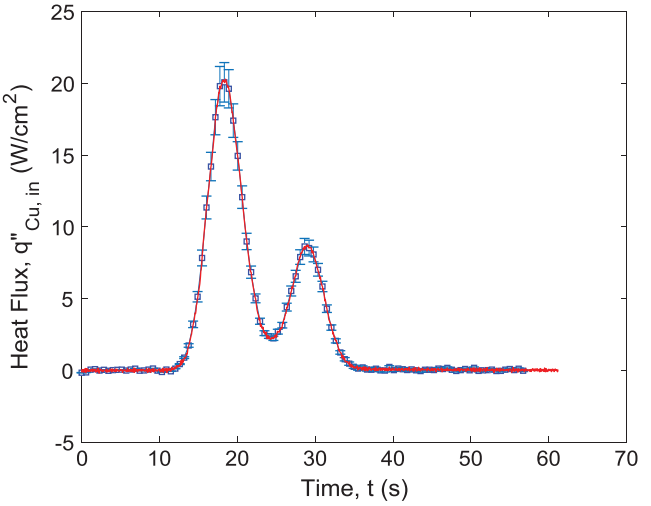

Fig. 34 Estimated incoming copper heat flux with uncertainty bars.

IV. Conclusions

This preliminary study suggests a procedural and experimental design process as well as a physical test cell for producing a reliable, repeatable, and accurate heat flux source. The design space envelope (heat flux in Watts per square meter, temperature in degrees Celsius, and heating rate in degrees Celsius per second) requires further consideration and expansion. Another important feature demonstrated here involves system costs and a rapid turnaround process. A 90 W/cm^2 heat flux can be demonstrated on a stainless-steel sample for a short period of time as the present heater has a temperature limit of 450°C. It should be noted that higher temperature and heat flux heaters are presently being developed based on aluminum nitride substrates [38].

With these encouraging preliminary results, additional model and sensor improvements can be proposed. Two obvious improvements involve the heater-sample contact region and modeling of the heat loss into the insulation. First, alternative interfacial pastes and interface options should be pursued as well as consideration of energy storage in these materials. Second, the assumption of constant thermophysical properties in the insulation should be reconsidered. It is difficult to measure the insulation surface temperature $T_{\mathrm{INS}}(t)$. Therefore, the assumption $T_{\mathrm{AlN}}(t) = T_{\mathrm{INS}}(t)$ remains until an instrumentation solution is devised. Clearly this issue also arises in the insulation region about the copper slug where $T_{\mathrm{Cu}}(t) = T_{\mathrm{INS}}(t)$ is assumed. Frankel et al. [61] derived the transient heat-flux–surface-temperature relationship for a one-dimensional, semi-infinite geometry in an opaque material with known thermal conductivity (but constant thermal diffusivity). The derived relationship incorporated the Kirchhoff and Fourier cosine transforms [61]. Further remarks on these issues are presented in Ref. [62].

Acknowledgment

Support for this research is obtained from NSF-CBET-1703442.

References

[1] Diller, T. E., *Advances in Heat Flux Measurements*, Vol. 23, Academic Press, New York, 1993, pp. 279–368.

[2] Lu, F. K., and Marren, D. E., *Advanced Hypersonic Test Facilities*, Vol. 198, AIAA, Reston, VA, 2002, pp. 279–314.

[3] Cook, W. J., and Felderman, E. J., "Reduction of Data from Thin-Film Heat-Transfer Gages—A Concise Numerical Technique," *AIAA Journal*, Vol. 4, No. 3, 1966, pp. 561–562. doi:10.2514/3.3486

[4] Lu, F. K., and Kinnear, K. M., "Characterization of Thin-Film Heat-Flux Gauges," *Journal of Thermophysics and Heat Transfer*, Vol. 13, No. 4, 1999, pp. 548–549. doi:10.2514/2.6477

[5] Savino, R., Fumo, M. D. S., Silvestroni, L., and Sciti, D., "Arc-Jet Testing on HfB_2 and HfC-Based Ultra-High Temperature Ceramic Materials," *Journal of the European Ceramic Society*, Vol. 28, No. 9, 2008, pp. 1899–1907. doi:10.1016/j.jeurceramsoc.2007.11.021

[6] Candane, S. R., Balaji, C., and Venkateshan, S., "Ablation and Aero-Thermodynamic Studies on Thermal Protection Systems of Sharp-Nosed Re-Entry Vehicles," *Journal of Heat Transfer*, Vol. 129, No. 7, 2007, pp. 912–916. doi:10.1115/1.2717250

[7] Powars, C. A., Kennedy, W. S., and Rindal, R. A., "Heat Flux Measurement Using Swept Null Point Calorimetry," *Journal Spacecraft and Rockets*, Vol. 9, No. 9, 1972, pp. 668–672. doi:10.2514/3.61773

[8] Polezhaev, Y. V., "Modern Problems of Thermal Protection," *Journal of Engineering Physics and Thermophysics*, Vol. 74, No. 6, 2001, pp. 1364–1374. doi:10.1023/A:1013988030453

[9] Piccini, E., Guo, S. M., and Jones, T. V., "The Development of a New Direct-Heat-Flux Gauge for Heat-Transfer Facilities," *Measurement Science and Technology*, Vol. 11, No. 4, 2000, pp. 342–349. doi:10.1088/0957-0233/11/4/302

[10] Loehle, S., Battaglia, J. L., Batsale, J. C., Bourserau, F., Conte, D., Jullien, P., Van Ootegem, B., Couzi, J., and Lasserre, J. P., "Estimation of High Heat Flux in Supersonic Plasma Flows," *32nd Annual Conference on IEEE Industrial Electronics*, Vol. 4, IEEE Publ., Piscataway, NJ, 2006, pp. 5366–5373.

[11] Loehle, S., Battaglia, J. L., Batsale, J. C., Enouf, O., Dubard, J., and Filtz, J. R., "Characterization of a Heat Flux Sensor Using Short Pulse Laser Calibration," *Review of Scientific Instruments*, Vol. 78, No. 5, 2007, Paper 05301. doi:10.1063/1.2736388

[12] Beck, J. V., Blackwell, B., and Clair, C. R. S., Jr., *Inverse Heat Conduction: Ill-Posed Problems*, Wiley, New York, 1985, Chaps. 1, 2.

[13] Ozisik, M. N., and Orlande, H. R. B., *Inverse Heat Transfer: Fundamentals and Applications*, Taylor and Francis, New York, 2000, Chaps. 1, 2.

[14] Kurpisz, K., and Nowak, A., *Inverse Thermal Problems*, Computational Mechanics Publ., Southampton, England, U.K., 1995, Chap. 1, 2.

[15] Kress, R., *Linear Integral Equations*, 3rd ed., Springer-Verlag, New York, 1989, Chaps. 15–17.

[16] Linz, P., *Analytical and Numerical Methods for Volterra Equations*, Soc. for Industrial and Applied Mathematics, Philadelphia, 1985, Chaps. 5, 6, 8, 10.

[17] Wing, G. M., *A Primer on Integral Equations of the First Kind*, Soc. for Industrial and Applied Mathematics, Philadelphia, 1991, Chap. 3.

[18] Woodbury, K. A., "Effect of Thermocouple Sensor Dynamics on Surface Heat Flux Predictions Obtained via Inverse Heat Transfer Analysis," *International Journal of Heat and Mass Transfer*, Vol. 33, No. 12, 1990, pp. 2641–2649. doi:10.1016/0017-9310(90)90200-E

[19] Frankel, J., Elkins, B., and Keyhani, M., "Rate-Based Sensing Concepts for Heat Flux and Property Estimation; and, Transition Detection," *16th AIAA/DLR/DGLR International Space Planes and Hypersonic Systems and Technologies Conference*, AIAA Paper 2009-7303, Oct. 2009.

[20] Blanchat, T., Humphries, L., and Gill, W., "Sandia Heat Flux Gauge Thermal Response and Certainty Models," Sandia National Lab. Rept. SAND2000-1111, Albuquerque, NM, 2000.

[21] Elkins, B. S., Keyhani, M., and Frankel, J. I., "Surface Heat Flux Prediction Through Physics-Based Calibration, Part 2: Experimental Validation," *Journal of Thermophysics and Heat Transfer*, Vol. 27, No. 2, 2013, pp. 206–216. doi:10.2514/1.T3918

[22] Frankel, J. I., Keyhani, M., and Elkins, B. E., "Surface Heat Flux Prediction Through Physics-Based Calibration, Part 1: Theory," *Journal of Thermophysics and Heat Transfer*, Vol. 27, No. 2, 2013, pp. 189–205. doi:10.2514/1.T3917

[23] Frankel, J., and Keyhani, M., "Phase-Plane and Cross-Correlation Analysis for Estimating Optimal Regularization in Inverse Heat Conduction," *Journal of Thermophysics and Heat Transfer*, Vol. 28, No. 3, 2014, pp. 542–548. doi:10.2514/1.T4357

[24] Frankel, J. I., and Bottländer, D., "Acoustic Interferometry and the Calibration Integral Equation Method for Inverse Heat Conduction," *Journal of Thermophysics and Heat Transfer*, Vol. 29, No. 4, 2015, pp. 862–869. doi:10.2514/1.T4560

[25] Frankel, J. I., and Keyhani, M., "Nonlinear Inverse Calibration Heat Conduction Through Property Physics," *Journal of Thermophysics and Heat Transfer*, Vol. 28, No. 2, 2014, pp. 203–217. doi:10.2514/1.T4269

[26] Chen, H. C., Frankel, J. I., and Keyhani, M., "Nonlinear Inverse Heat Conduction Problem of Surface Temperature Estimation by Calibration Integral Equation Method," *Numerical Heat Transfer, Part B: Fundamentals*, Vol. 73, No. 5, 2018, pp. 263–291. doi:10.1080/10407790.2018.1464316

[27] Chen, H. C., Frankel, J. I., and Keyhani, M., "Two-Probe Calibration Integral Equation Method for Nonlinear Inverse Heat Conduction Problem of Surface Heat Flux Estimation," *International Journal of Heat and Mass Transfer*, Vol. 121, June 2018, pp. 246–264. doi:10.1016/j.ijheatmasstransfer.2017.12.072

[28] Chen, Y. Y., Frankel, J. I., and Keyhani, M., "Nonlinear, Rescaling-Based Inverse Heat Conduction Calibration Method and Optimal Regularization Parameter Strategy," *Journal of Thermophysics and Heat Transfer*, Vol. 30, No. 1, 2016, pp. 67–88. doi:10.2514/1.T4572

[29] Chen, Y. Y., Frankel, J. I., and Keyhani, M., "A New Front Surface Heat Flux Calibration Method for a 1-D Nonlinear Thermal System with a Time-Varying Back Boundary Condition," *Journal of Engineering Mathematics*, Vol. 105, No. 1, 2017, pp. 157–187. doi:10.1007/s10665-016-9888-0

[30] Myrick, J. A., Keyhani, M., and Frankel, J. I., "Determination of Surface Heat Flux and Temperature Using in-Depth Temperature Data–Experimental Verification," *International Journal of Heat and Mass*

Transfer, Vol. 111, 2017, pp. 982–998.
doi:10.1016/j.ijheatmasstransfer.2017.04.029
[31] Myrick, J. A., Keyhani, M., and Frankel, J. I., "Inverse Prediction of Temperature Through Time Rescaling of High-Temperature Experimental Data," *Journal of Thermal Science and Engineering Applications*, Vol. 8, No. 4, 2016, Paper 041005.
doi:10.1115/1.4034093
[32] Battaglia, J.-L., Cois, O., Puigsegur, L., and Oustaloup, A., "Solving an Inverse Heat Conduction Problem Using a Non-Integer Identified Model," *International Journal of Heat and Mass Transfer*, Vol. 44, No. 14, 2001, pp. 2671–2680.
doi:10.1016/S0017-9310(00)00310-0
[33] Gardarein, J. L., Battaglia, J. L., and Loehle, S., "Heat Flux Sensor Calibration Using Noninteger System Identification: Theory, Experiment, and Error Analysis," *Review of Scientific Instruments*, Vol. 80, No. 2, 2009, Paper 025103.
doi:10.1063/1.3079328
[34] Loehle, S., Battaglia, J. L., Jullien, P., Van Ootegem, B., Couzi, J., and Lasserre, J. P., "Improvement of High Heat Flux Measurement Using a Null-Point Calorimeter," *Journal of Spacecraft and Rockets*, Vol. 45, No. 1, 2008, pp. 76–81.
doi:10.2514/1.30092
[35] Loehle, S., and Frankel, J. I., "Physical Insight into System Identification Parameters Applied to Inverse Heat Conduction Problems," *Journal of Thermophysics and Heat Transfer*, Vol. 29, No. 3, 2015, pp. 467–472.
doi:10.2514/1.T4431
[36] Blanchat, T. K., and Hanks, C. R., "Comparison of the High Temperature Heat Flux Sensor to Traditional Heat Flux Gages Under High Heat Flux Conditions," Sandia National Lab. Rept. SAND2012-10683, Albuquerque, NM, 2013.
[37] http://oasismaterials.com [retrieved 15 June 2016].
[38] https://durexindustries.com/aluminum-nitride-and-alumina-ceramic-heaters [retrieved 20 June 2016].
[39] Ho, C. K., Mahoney, A. R., Ambrosini, A., Bencomo, M., Hall, A., and Lambert, T. N., "Characterization of Pyromark 2500 Paint for High-Temperature Solar Receivers," *Journal of Solar Energy Engineering–Transactions of the ASME*, Vol. 136, No. 1, 2014, Paper 041005.
doi:10.1115/1.4024031
[40] http://www.aerogel.com/products-and-solutions/all-insulation-products [retrieved 21 Aug. 2015].
[41] http://www.datatranslation.eu/nz/measure/strain-measurement/dt9829/multi-sensor-measurement,1465.html?merk=7c5179ca821481705e28677cccf623ad [retrieved 10 Jan. 2016].
[42] https://www.keysight.com/en/pc-856751/n5700-and-n8700-series-dc-system-power-supplies-gpib-single-output?cc=US&lc=eng [retrieved 24 Aug. 2016].
[43] https://www.coleparmer.com/i/cole-parmer-stabletemp-ceramic-hot-plate-10-x-10-120-vac/0340530 [retrieved 09 April 2015].
[44] https://www.zircarceramics.com/product/microsil [retrieved 30 Aug. 2016].
[45] http://www.omega.com/pptst/CO-K.html [retrieved 22 Feb. 2017].
[46] http://www.omega.com/pptst/EXGG-2CU_3CU_WIRE.html [retrieved 02 Oct. 2016].
[47] "Series No. TMTIN-020E-3," http://www.omega.com [retrieved 02 Oct. 2016].
[48] http://www.ioffe.ru/SVA/NSM/Semicond/AlN/thermal.html [retrieved 09 Aug. 2016].
[49] Koshchenko, V. I., Grinberg, Y. K., and Demidenko, A. F., "Thermodynamic properties of AlN (5-2700 K), GaP (5-1500 K) and BP (5-800 K)," Izv. Akad. Nauk SSSR, Neorg. Mater, Vol. 20, No. 11, 1984, pp. 1787–1790.
[50] https://datatranslation.box.com/shared/static/mvsso9i9tydmzawp5luy.pdf [retrieved 10 Aug. 2016].
[51] Beck, J. V., and Arnold, K. J., *Parameter Estimation*, Wiley, New York, 1977, p. 411.
[52] Figueroa, V. A., Nakos, J. T., and Murphy, J. E., "Uncertainty Analysis of Heat Flux Measurements Estimated Using One-Dimensional Inverse Heat Conduction Program," Sandia National Lab. Rept. SAND2005-0039, Albuquerque, NM, 2005.
[53] Incropera, F. P., DeWitt, D. P., Bergman, T. L., and Lavine, A. S., *Fundamentals of Heat and Mass Transfer*, 6th ed., Wiley, New York, 2006, Appendix A.
[54] Abu-Eishah, S. I., Haddad, Y., Solieman, A., and Bajbouj, A., "A New Correlation for the Specific Heat of Metals, Metal Oxides and Metal Fluorides as a Function of Temperature," *Latin American Applied Research*, Vol. 34, No. 4, 2004, pp. 257–265.
[55] Taylor, B. N., "Guidelines for Evaluating and Expressing the Uncertainty of NIST Measurement Results," National Inst. of Standards and Technology, TN 1297, Gaithersburg, MD, 1994.
[56] Hills, R. G., and Trucano, T. G., "Statistical Validation of Engineering and Scientific Models: Background," Sandia National Lab. Rept. SAND99-1256, Albuquerque, NM, 1999.
[57] Stern, F., Muste, M., Beninati, M.-L., and Eichinger, W. E., "Summary of Experimental Uncertainty Assessment Methodology with Example," Iowa Inst. of Hydraulic Research, Univ. of Iowa, TR 406, Iowa City, IA, 1999.
[58] Coleman, H. W., and Steele, W. G., "Engineering Application of Experimental Uncertainty Analysis," *AIAA Journal*, Vol. 33, No. 10, 1995, pp. 1888–1896.
doi:10.2514/3.12742
[59] Moffat, R. J., "Describing the Uncertainties in Experimental Results," *Experimental Thermal and Fluid Science*, Vol. 1, No. 1, 1988, pp. 3–17.
doi:10.1016/0894-1777(88)90043-X
[60] Bryant, R., Womeldorf, C., Johnsson, E., and Ohlemiller, T., "Radiative Heat Flux Measurement Uncertainty," *Fire and Materials*, Vol. 27, No. 5, 2003, pp. 209–222.
doi:10.1002/(ISSN)1099-1018
[61] Frankel, J., Keyhani, M., and Huang, M., "Local Sensitivity Analysis for the Heat Flux-Temperature Integral Relationship in the Half-Space," *Applied Mathematics and Computation*, Vol. 217, No. 1, 2010, pp. 363–375.
doi:10.1016/j.amc.2010.05.070
[62] Frankel, J. I., Chen, H., Mathew, K., and Bottländer, D., "Rigorous Characterization of an Advanced Instrumented Aluminum Nitride (AlN) Electrical Heater for High-Heat Flux and High-Temperature Aerospace Applications," *2018 AIAA Aerospace Sciences Meeting*, AIAA Paper 2018-0983, Jan. 2018.